

# Image Response Regression via Deep Neural Networks

Daiwei Zhang<sup>1,2</sup>, Lexin Li<sup>3</sup>, Chandra Sripada<sup>1</sup>, and Jian Kang<sup>1,\*</sup>

<sup>1</sup>University of Michigan, Ann Arbor

<sup>2</sup>University of Pennsylvania

<sup>3</sup>University of California, Berkeley

\*Corresponding author. Email: jiankang@umich.edu

March 4, 2022

## Abstract

Delineating the associations between images and a vector of covariates is of central interest in medical imaging studies. To tackle this problem of image response regression, we propose a novel nonparametric approach in the framework of spatially varying coefficient models, where the spatially varying functions are estimated through deep neural networks. Compared to existing solutions, the proposed method explicitly accounts for spatial smoothness and subject heterogeneity, has straightforward interpretations, and is highly flexible and accurate in capturing complex association patterns. A key idea in our approach is to treat the image voxels as the effective samples, which not only alleviates the limited sample size issue that haunts the majority of medical imaging studies, but also leads to more robust and reproducible results. Focusing on a broad family of piecewise smooth functions, we establish the estimation and selection consistency, and derive the asymptotic error bounds. We demonstrate the efficacy of the method through intensive simulations, and further illustrate its advantages with analyses of two functional magnetic resonance imaging datasets.

## 1 Introduction

A central question in medical imaging studies is to delineate the associations between images and a set of covariates, such as demographics and clinical features. For instance, anatomical magnetic resonance imaging (MRI) studies can be conducted to locate brain regions exhibiting structural differences between normal controls and patients with neurological disorders, after accounting for demographic covariates. Another example is functional magnetic resonance imaging (fMRI) studies for identifying brain locations that demonstrate differential activation patterns under different tasks. These examples can be collectively formulated as a regression problem where the image scans, usually measured over a two- or three-dimensional spatial space, are treated as the response variable, while the demographic and clinical features are treated as the predictors. We refer to this type of analysis as the image response regression.

Image response regression involves multiple challenges. First, the image dimensions are ultrahigh. For instance, a  $64 \times 64 \times 64$  MRI image records data over  $64^3 = 262,144$  voxels. Meanwhile, complex spatial correlations exist among imaging voxels and regions. Second, the association patterns between images and covariates can be highly complex, as imaging signals are often found in contiguous, sharp-edged regions that are sparsely distributed throughout the spatial volume (Chumbley and Friston, 2009), which is exacerbated by a high noise level, all of which leads to a low signal-to-noise ratio. Third, while a typical imaging study collects data from multiple subjects, the number of subjects is usually limited (mostly in the order of tens or hundreds) compared to the ultrahigh dimensionality of the image, with subject-specific heterogeneity being the rule rather than the exception. To address those challenges, there have been several lines of research proposed for image response regression.

The first and perhaps the most common solution is the mass univariate analysis (Friston, 2003, MUA), which fits a generalized linear model to associate the image measure at each voxel with the covariates. A major limitation of MUA is that the model is fitted one voxel at a time, without accounting for spatial correlations, which often leads to low detection power. To partially overcome this limitation, there have been proposals of pre-smoothing (Friston, 2003), or adaptive smoothing (Qiu, 2007; Yue et al., 2010)

to incorporate neighboring voxel information. Nevertheless, it remains challenging to capture complex associations between images and covariates, as well as subject heterogeneity.

The second line of research treats the image as a tensor, i.e., a multi-dimensional array, and then fits a tensor response regression model under different low-rank and sparsity structures (Rabusseau and Kadri, 2016; Li and Zhang, 2017; Sun and Li, 2017; Raskutti et al., 2019; Chen et al., 2019). These solutions implicitly accounts for spatial smoothness, but usually not subject heterogeneity. Moreover, due to the limited sample size, large noise, and computational constraints, the response images are often downsized to a smaller dimension to reach a compromise between model accuracy and feasibility.

A third strategy is to utilize a spatially varying coefficient model, where the response images and the regression coefficients are modeled as the realizations of some spatially varying functions evaluated on discrete grid points, i.e., voxels, in a spatial domain. This family of solutions systematically incorporate spatial smoothness, jump discontinuities, and subject-specific heterogeneity, and have been shown to be highly effective in characterizing the image-covariate associations. Notably, Zhu et al. (2014) developed the spatially varying coefficient model for neuroimaging data with jump discontinuities. They employed local linear regression and functional principal components to estimate the coefficient functions, and developed an asymptotic Wald test to identify significant association regions. Chen et al. (2016) extended the model of Zhu et al. (2014), by coupling with an  $L_1$  type penalty for sparsity, and a total variation type penalty for spatial contiguity. Li et al. (2017) introduced a single-index structure into the model, and iteratively estimated varying coefficient functions, link functions, index parameter vectors, and the covariance function of individual functions. Alternatively, Li et al. (2020) and Yu et al. (2020) considered a version of the spatially varying coefficient model where the image is located in a two-dimensional space, but the covariates can be ultrahigh-dimensional. They employed bivariate splines over triangulation to approximate the coefficient functions, and added the adaptive  $L_1$  penalty for simultaneous sparse learning and model structure identification. From a Bayesian perspective, Shi and Kang (2015) used thresholded multiscale Gaussian processes, while Bussas et al. (2017) used Gaussian processes with isotropic priors, to model the spatially varying functions.

In recent years, a family of machine learning methods based upon deep neural networks (DNN) have enjoyed enormous success in a wide range of applications, among which medical imaging analysis is a particularly remarkable example (LeCun et al., 2015; Goodfellow et al., 2016). Such success can be attributed to the expressive power of DNN in approximating and learning highly complex nonparametric models (Fan et al., 2019). In fact, any continuous function on a compact set can be approximated by a single-hidden layer neural network with a sufficiently large number of nodes to an arbitrary degree of accuracy (Barron, 1994). Meanwhile, in terms of the required total number of nodes, a deeper neural network, i.e., one with more hidden layers, has been shown to be more efficient in approximating functions than a shallower one (Telgarsky, 2016; Eldan and Shamir, 2016). Recently, studies have investigated the convergence rate of multi-layer neural networks. Notably, Barron (1994); McCaffrey and Gallant (1994) obtained the convergence rate for a single-layer neural network. Kohler and Krzyżak (2017) established the minimax convergence rate for a two-layer network. Bauer et al. (2019) extended this result to a multi-layer network with a smooth activation function, whereas Schmidt-Hieber et al. (2020) proved a similar result for a rectified linear unit (ReLU) activation function. Other studies have investigated variable selection in DNN. Notably, Feng and Simon (2017) imposed a group  $L_1$  penalty on the weights of the first layer, while Chen et al. (2020) introduced an additional selection layer to select relevant input variables.

Despite the wide success of DNN in medical imaging analysis, numerous challenges remain, one of which is the limited sample size. DNN training typically requires a fairly large sample size, while most medical imaging studies only enroll a small number of subjects. As a result, a successful application of DNN in medical imaging always requires intensive and arduous tuning of the architecture and parameters of the neural network, and is often difficult to reproduce. Aggregating multiple imaging centers to reach a large sample size is a viable solution, but at the cost of introducing center-specific variability. In addition, how to interpret the DNN model and how to handle data heterogeneity in DNN remain partially addressed only.

In this article, we propose a novel image response regression approach that integrates spatially varying coefficient models with deep neural networks. That is, we adopt the spatially varying coefficient model framework similar to that of Zhu et al. (2014); Li et al. (2020), but we estimate the functions of main effect, individual deviation, and error variance all through multi-layer neural networks. Our approach enjoys several advantages. Compared to the massive univariate analysis or tensor response regressions,

our method explicitly accounts for both spatial smoothness and subject heterogeneity. We achieve the former by focusing our candidate functions in a piecewise smooth function class, and the latter by including and estimating an individual deviation function specific for each subject. Compared to the spatially varying coefficient models based on local linear regression or bivariate splines, our DNN-based model is more flexible and able to capture more complex association patterns, thanks to the approximation capability of DNNs. Moreover, we treat each subject-specific deviation function as a fixed target, rather than a random effect term, and estimate it directly, which allows a more direct characterization of the subject-specific heterogeneity. This treatment differentiates our proposal from alternative varying coefficient model-based solutions such as Zhu et al. (2014); Li et al. (2020). Compared to the vast DNN-based medical imaging analysis literature, our model is straightforward to interpret, as we use DNNs to approximate the main effect, individual deviation, and error variance functions, while their interpretations remain the same as in a classical varying coefficient model. To further improve the interpretability of the main effect function, we impose sparsity on the entire function, but *not* on the parameters of the fitted neural networks, bypassing the interpretation and selection of those individual parameters, which can be difficult. In addition, a key innovation of our proposal is that, when fitting the neural networks to those functions, we treat each spatial coordinate as a sample observation. Consequently, the effective sample size is no longer the number of subjects, but rather the total number of voxels, which is typically much larger. This strategy leads to a more accurate DNN fit to the data and a more robust and reproducible performance with respect to the architecture of the DNNs, which is confirmed by our empirical studies.

Our proposal makes several useful contributions. We extend the family of spatially varying coefficient models to address an important class of scientific problems of image response regression. Our model is able to capture a wide variety of spatial correlation patterns, including both smooth transitions, as well as jump discontinuities. We also extend the theory of nonparametric regression modeling. We derive the asymptotic convergence rate of the estimated functions, and establish the selection consistency of the sparse function, as either the number of voxels or the number of subjects diverges to infinity. We derive the asymptotic error bound, not only for globally smooth functions, but also for a broader family of piecewise smooth generalized hierarchical interaction functions, and show that the bound is comparable to the minimax bound in the traditional nonparametric regressions. Finally, our proposal exemplifies how to utilize state-of-the-art deep learning tools to help address a classical statistical problem, which enjoys both modeling flexibility and theoretical guarantees.

The rest of the article is organized as follows. We present the model and the DNN-based estimation method in Section 2, followed by a study of their theoretical properties in Section 3. We evaluate the empirical performance of our approach compared with alternative solutions in Section 4, and apply them to two brain imaging datasets in Section 5. Section 6 concludes the article with a discussion. All technical proofs are relegated to the Supplementary Materials.

## 2 Model and Estimation

In this section, we first present the image response regression through the spatially varying coefficient model. We next propose to estimate the key functions in the model using deep neural networks, and derive a multi-step estimation procedure.

### 2.1 Image response regression with spatially varying coefficients

Suppose the imaging data are collected from a  $D$ -dimensional compact space  $\mathcal{S} \subset \mathbb{R}^D$  observed at  $V$  spatial locations, along with  $J$  covariates, from  $N$  individual subjects. For each subject  $i = 1, \dots, N$ , let  $y_i(\mathbf{s}_v) \in \mathbb{R}$  denote the image measurement at the spatial location  $\mathbf{s}_v \in \mathcal{S}, v = 1, \dots, V$ , and let  $\mathcal{S}_V = \{\mathbf{s}_v\}_{v=1}^V$  collect all those locations. Let  $\mathbf{x}_i = (x_{i1}, \dots, x_{iJ})^\top \in \mathbb{R}^J$  denote the  $J$ -dimensional covariate vector. We consider the following spatially varying coefficient model,

$$y_i(\mathbf{s}_v) = \sum_{j=1}^J x_{ij} \beta_j(\mathbf{s}_v) + \alpha_i(\mathbf{s}_v) + \epsilon_i(\mathbf{s}_v), \quad i = 1, \dots, N, v = 1, \dots, V, \quad (1)$$

where  $\beta_j(\mathbf{s}_v) \in \mathbb{R}$  characterizes the main effect of the  $j$ th covariate  $x_{ij}$  common for all subjects  $i$ ,  $\alpha_i(\mathbf{s}_v) \in \mathbb{R}$  characterizes the individual deviation from the common main effect that is specific to subject

$i$ , and  $\epsilon_i(\mathbf{s}_v) \in \mathbb{R}$  is the measurement error that is assumed to have mean zero, variance  $\sigma^2(\mathbf{s}_v) > 0$ , and  $\epsilon_i(\mathbf{s}_v)$  is independent of  $\epsilon_{i'}(\mathbf{s}_{v'})$  whenever  $i \neq i'$  or  $v \neq v'$  for  $i, i' \in \{1, \dots, N\}$  and,  $v, v' \in \{1, \dots, V\}$ .

In model (1), we view  $\beta_j(\mathbf{s}_v), \alpha_i(\mathbf{s}_v), \sigma^2(\mathbf{s}_v)$  as the realizations of the functions  $\beta_j(\mathbf{s}), \alpha_i(\mathbf{s}), \sigma^2(\mathbf{s})$  at the set of spatial locations  $\{\mathbf{s}_v\}_{v=1}^V$ . In addition, we note that the individual deviation  $\alpha_i(\mathbf{s}_v)$  plays a similar role as the random effect term in the spatially varying coefficient model in Zhu et al. (2014); Li et al. (2020). However, a key difference is that in their works,  $\alpha_i(\mathbf{s}_v)$  are assumed to be copies of a stochastic process, whose covariance structure is to be estimated, whereas in our context, each  $\alpha_i(\mathbf{s}_v)$  is treated as a realization of a deterministic function, and that function itself is to be estimated directly. Finally, since the error variance  $\sigma^2(\mathbf{s}_v)$  is also a function of  $\mathbf{s}_v$ , we can flexibly capture the spatial heterogeneity with respect to the degree of variation in the measurement error.

Write  $\boldsymbol{\beta}(\mathbf{s}) = (\beta_1(\mathbf{s}), \dots, \beta_J(\mathbf{s}))^\top \in \mathbb{R}^J$ , and  $\boldsymbol{\alpha}(\mathbf{s}) = (\alpha_1(\mathbf{s}), \dots, \alpha_N(\mathbf{s}))^\top \in \mathbb{R}^N$ . We outline some requirements for  $\boldsymbol{\beta}(\mathbf{s}), \boldsymbol{\alpha}(\mathbf{s}), \sigma^2(\mathbf{s})$  to ensure the identifiability and interpretability of model (1). We give more rigorous definitions in Section 3. Specifically, we require that the functions  $\boldsymbol{\beta}(\mathbf{s}), \boldsymbol{\alpha}(\mathbf{s}), \sigma^2(\mathbf{s})$  are all *piecewise* smooth with a finite number of continuous components. In addition, we impose some form of sparsity, in the sense that, for each covariate  $x_j$ , there are image regions where the main effect equals zero, and the absolute value of the nonzero main effects have a positive constant lower bound. Similar conditions have been adopted in the imaging analysis literature (e.g., Zhu et al., 2014; Sun and Li, 2017; Li et al., 2020).

## 2.2 Approximation via deep neural networks

We propose to approximate the functions  $\boldsymbol{\beta}(\mathbf{s}), \boldsymbol{\alpha}(\mathbf{s}), \sigma^2(\mathbf{s})$  in model (1) using deep neural networks. Specifically, we consider a general  $L$ -layer feed-forward neural network, where the dimension of the input layer is  $K_0$ , the dimension of the  $\ell$ th hidden layer is  $K_\ell$ ,  $\ell = 1, \dots, L$ , and the dimension of the output layer is  $K_{L+1}$ . That is, the  $\ell$ th hidden layer has  $K_\ell$  hidden nodes, which is often set to  $K_1 = \dots = K_L = K$ . For a  $K_0$ -dimensional vector input  $\mathbf{s} \in \mathbb{R}^{K_0}$ , the function produced by this neural network is of the form,

$$\mathcal{N}(\mathbf{s} \mid \boldsymbol{\theta}) = \mathbf{W}_L \phi_L \left( \dots \mathbf{W}_1 \phi_1 (\mathbf{W}_0 \mathbf{s} + \mathbf{b}_0) + \mathbf{b}_1 \dots \right) + \mathbf{b}_L, \quad (2)$$

where  $\mathbf{W}_\ell \in \mathbb{R}^{K_{\ell+1} \times K_\ell}$  and  $\mathbf{b}_\ell \in \mathbb{R}^{K_{\ell+1}}$  are the weight and bias parameters from the  $\ell$ th hidden layer to the  $(\ell + 1)$ th hidden layer,  $\ell = 0, \dots, L$ , and  $\boldsymbol{\theta} = \{\mathbf{W}_\ell, \mathbf{b}_\ell\}_{\ell=0}^L$  collects all the parameters. The function  $\phi_\ell(\cdot)$  is a vector-valued nonlinear activation function, where the activation is applied to each element of the  $K_\ell$ -dimensional input vector, and the output is another  $K_\ell$ -dimensional vector,  $\ell = 1, \dots, L$ . Common choices of the activation include the sigmoid function  $\{1 + \exp(u)^{-1}\}^{-1}$ , and the rectified linear unit (ReLU) function  $\max(0, u)$ .

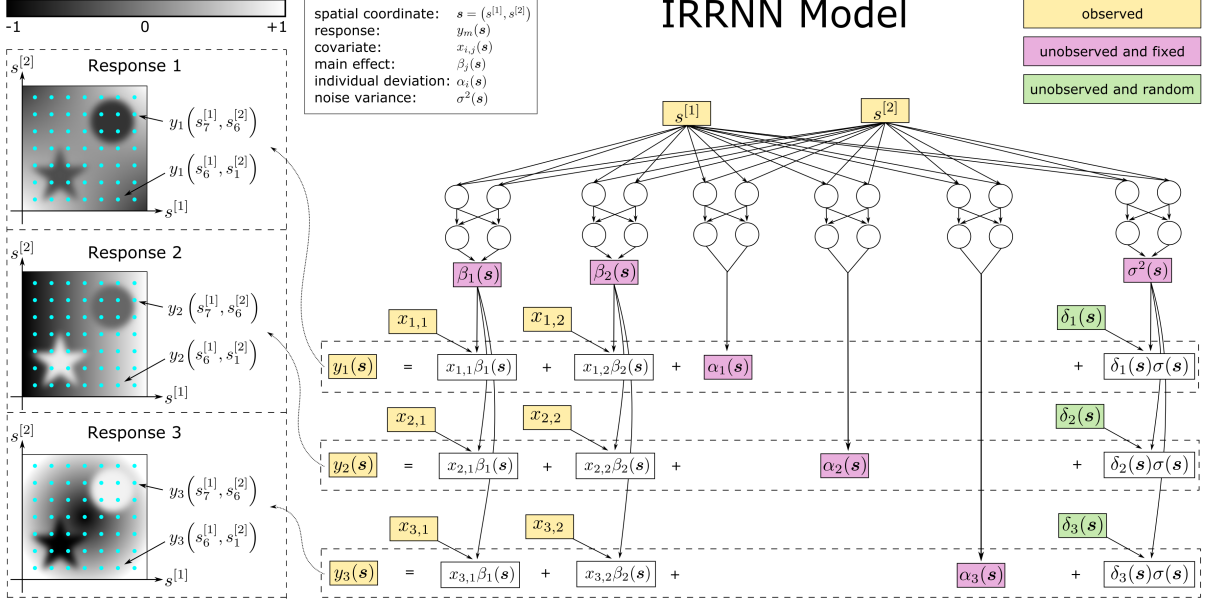
We then approximate  $\boldsymbol{\beta}(\mathbf{s}), \boldsymbol{\alpha}(\mathbf{s}), \sigma^2(\mathbf{s})$  using the neural network in (2) as,

$$\boldsymbol{\beta}(\mathbf{s}) \approx \mathcal{N}_\beta(\mathbf{s} \mid \boldsymbol{\theta}_\beta), \quad \boldsymbol{\alpha}(\mathbf{s}) \approx \mathcal{N}_\alpha(\mathbf{s} \mid \boldsymbol{\theta}_\alpha), \quad \log\{\sigma^2(\mathbf{s})\} \approx \mathcal{N}_\sigma(\mathbf{s} \mid \boldsymbol{\theta}_\sigma). \quad (3)$$

The output of the neural networks in (3), i.e.,  $\mathcal{N}_\beta(\mathbf{s} \mid \boldsymbol{\theta}_\beta)$ ,  $\mathcal{N}_\alpha(\mathbf{s} \mid \boldsymbol{\theta}_\alpha)$ , and  $\mathcal{N}_\sigma(\mathbf{s} \mid \boldsymbol{\theta}_\sigma)$ , is of dimension  $J$ ,  $N$ , and 1, respectively. That is,  $\mathcal{N}_\beta(\mathbf{s} \mid \boldsymbol{\theta}_\beta) = [\mathcal{N}_{\beta_1}(\mathbf{s} \mid \boldsymbol{\theta}_{\beta_1}), \dots, \mathcal{N}_{\beta_J}(\mathbf{s} \mid \boldsymbol{\theta}_{\beta_J})]^\top$  is a concatenation of  $J$  neural networks, and  $\mathcal{N}_\alpha(\mathbf{s} \mid \boldsymbol{\theta}_\alpha) = [\mathcal{N}_{\alpha_1}(\mathbf{s} \mid \boldsymbol{\theta}_{\alpha_1}), \dots, \mathcal{N}_{\alpha_N}(\mathbf{s} \mid \boldsymbol{\theta}_{\alpha_N})]^\top$  is a concatenation of  $N$  neural networks. The input of the neural networks in (3) is the  $D$ -dimensional spatial coordinate,  $\mathbf{s}_v \in \mathcal{S} \subset \mathbb{R}^D, v = 1, \dots, V$ , which consists of the same fixed design points for all neural networks. In that regard, the model fitting with (3) is similar to classical regression with fixed-design predictors. For a 3-dimensional image, the input dimension is  $D = 3$ . Figure 1 gives a graphic illustration of the architecture of our proposed method.

There are several advantages of using (3) to estimate the unknown functions in model (1). First, the neural network is highly flexible in capturing complex patterns of the spatially varying coefficient functions. Second, the interpretation of the functions  $\boldsymbol{\beta}(\mathbf{s}), \boldsymbol{\alpha}(\mathbf{s}), \sigma^2(\mathbf{s})$  remains the same as in the classical varying coefficient model. We do not need to interpret the individual parameters  $\boldsymbol{\theta}_\beta, \boldsymbol{\theta}_\alpha, \boldsymbol{\theta}_\sigma$  of those fitted neural nets. Moreover, to achieve sparsity to further facilitate the interpretation, we introduce hard thresholding to the main effect function  $\boldsymbol{\beta}(\mathbf{s})$ , but avoid imposing sparsity on  $\boldsymbol{\theta}_\beta$ . Finally, the effective sample size in (3) becomes the number of voxels, no longer the number of subjects. For brain images with typical resolutions, the number of voxels is easily in the order of hundreds of thousands or millions, which provides a sufficiently large effective sample size to train the deep neural networks in (3). In addition, coupled with low-dimensional input variables, our model fitting is relatively robust to the architecture of the neural network used, such as the number of hidden layers and hidden nodes.

Figure 1: Graphical illustration of the proposed method. In this example, the data contain  $J = 2$  covariates and  $N = 3$  images of dimension  $D = 2$ , observed on a grid of  $V = 7 \times 7$  voxels.



### 2.3 Estimation algorithm

We devise a three-step algorithm to estimate the functions  $\beta(\mathbf{s})$ ,  $\alpha(\mathbf{s})$ ,  $\sigma^2(\mathbf{s})$  in model (1). We also impose sparsity on the function  $\beta(\mathbf{s})$  to further improve the interpretability.

In Step 1, we estimate the main effect function  $\beta(\mathbf{s})$ . Write  $\mathbf{y}(\mathbf{s}_v) = (y_1(\mathbf{s}_v), \dots, y_N(\mathbf{s}_v))^T \in \mathbb{R}^N$ ,  $v = 1, \dots, V$ , and  $\mathbf{X} = (\mathbf{x}_1, \dots, \mathbf{x}_N)^T \in \mathbb{R}^{N \times J}$ . We first obtain an initial estimator of the error variance from the mean squared residuals of massive univariate regressions,

$$\tilde{\sigma}_v^2 = N^{-1} \left\| [\mathbf{I}_N - \mathbf{X}(\mathbf{X}^T \mathbf{X})^{-1} \mathbf{X}^T] \mathbf{y}(\mathbf{s}_v) \right\|_2^2, \quad v = 1, \dots, V,$$

where  $\mathbf{I}_N$  is the  $N \times N$  identity matrix.

We next estimate the main effect function, by fitting the neural network (2),

$$\hat{\theta}_\beta = \arg \min_{\theta_\beta} \sum_{v=1}^V \left\| \mathbf{y}(\mathbf{s}_v) - \mathbf{X} \mathcal{N}_\beta(\mathbf{s}_v | \theta_\beta) \right\|_2^2 \tilde{\sigma}_v^{-2} + \lambda \|\mathcal{N}(\mathbf{s}_v | \theta_\beta)\|_1, \quad (4)$$

where  $\lambda > 0$  is an  $L_1$  regularization parameter. We carry out the optimization in (4) by mini-batch stochastic gradient descent (Bottou, 2010, SGD), where, in our model, a mini-batch of samples in SGD corresponds to a subset of the voxels in  $\mathcal{S}_V$ . We denote the resulting estimator from (4) by  $\tilde{\beta}(\mathbf{s}) = \mathcal{N}_\beta(\mathbf{s} | \hat{\theta}_\beta)$ .

Next, we apply hard thresholding to the fitted main effect function, i.e.,

$$\hat{\beta}(\mathbf{s}_v) = \tilde{\beta}(\mathbf{s}_v) \otimes \mathbb{I} \left\{ |\tilde{\beta}(\mathbf{s}_v)| > \boldsymbol{\eta} \right\}, \quad (5)$$

where  $\mathbb{I}$  is the indicator function,  $\otimes$  is the Kronecker product, all operations are element-wise, and  $\boldsymbol{\eta} = (\eta_1, \dots, \eta_J)^T \in \mathbb{R}^J$  is the covariate-specific thresholding level. The use of the  $L_1$  regularization in (4) is to improve the empirical performance of the estimator, and the  $L_0$  regularization in (5) is to induce sparsity and facilitate selection. This procedure is similar to the thresholded Lasso (Zhou, 2010).

In Step 2, we estimate the individual deviation function  $\alpha(\mathbf{s})$ , by fitting (2),

$$\hat{\theta}_\alpha = \arg \min_{\theta_\alpha} \sum_{v=1}^V \left\| \mathbf{y}(\mathbf{s}_v) - \mathbf{X} \hat{\beta}(\mathbf{s}_v) - \mathcal{N}_\alpha(\mathbf{s}_v | \theta_\alpha) \right\|_2^2 \tilde{\sigma}_v^{-2}, \quad (6)$$

where the optimization is done by the mini-batch SGD again. We denote the resulting estimator from (6) by  $\hat{\alpha}(\mathbf{s}_v) = \mathcal{N}_\alpha(\mathbf{s}_v | \hat{\boldsymbol{\theta}}_\alpha)$ .

In Step 3, we estimate the error variance function  $\sigma^2(\mathbf{s})$ . We first update the mean squared residual estimator based on the estimated  $\hat{\boldsymbol{\beta}}(\mathbf{s})$  and  $\hat{\alpha}(\mathbf{s})$  as,

$$\bar{\sigma}_v^2 = N^{-1} \|\mathbf{y}(\mathbf{s}_v) - \mathbf{X}\hat{\boldsymbol{\beta}}(\mathbf{s}_v) - \hat{\alpha}(\mathbf{s}_v)\|_2^2, \quad v = 1, \dots, V.$$

We then estimate the error variance function  $\sigma^2(\mathbf{s})$ , by fitting the neural network (2),

$$\hat{\boldsymbol{\theta}}_\sigma = \arg \min_{\boldsymbol{\theta}_\sigma} \sum_{v=1}^V \|\bar{\sigma}_v^2 - \exp\{\mathcal{N}_\sigma(\mathbf{s}_v | \boldsymbol{\theta}_\sigma)\}\|_2^2, \quad (7)$$

where the optimization is done again by the mini-batch SGD. We denote the resulting estimator from (7) by  $\hat{\sigma}^2(\mathbf{s}_v) = \mathcal{N}_\sigma(\mathbf{s}_v | \hat{\boldsymbol{\theta}}_\sigma)$ .

Unlike iterative algorithms, the procedure above only goes through each step once, as, based on our numerical experiments, the estimate does not change much after the first iteration. The one-step estimation procedure also simplifies the subsequent theoretical analysis. Similar one-step estimation methods have been proposed before. For instance, Zhu et al. (2014) proposed a one-step estimator that sequentially estimates the main effect, individual deviation, and error variance, followed by smoothing and selection of the main effect estimate.

Our method involves two tuning parameters, the regularization parameter  $\lambda$  in (4), and the thresholding parameter  $\boldsymbol{\eta} = \{\eta_j\}_{j=1}^p$  in (5). To determine  $\lambda$ , we first adopt voxel-wise Lasso and identify  $\lambda_v$  that yields the smallest cross-validation error for that voxel. We then set  $\lambda$  as the median of  $\{\lambda_v\}_{v=1}^V$ . To determine  $\eta_j$ , we first carry out the mass univariate analysis, and choose  $\eta_j$ , such that  $\sum_{v=1}^V \mathbb{I}\{|\hat{\beta}_j(\mathbf{s}_v)| > \eta_j\} = \sum_{v=1}^V \mathbb{I}\{Z_j(\mathbf{s}_v) > z_{1-a/2}\}$ , where  $Z_j(\mathbf{s}_v)$  is the  $Z$ -statistic at location  $\mathbf{s}_v$  and  $z_{1-\alpha/2}$  is the  $(1 - a/2)$ th quantile of the standard normal distribution,  $\alpha = 0.05$ , and  $j = 1, \dots, J$ .

Regarding the architecture and implementation of the deep neural network employed in (2), we choose  $L = 4$  hidden layers, and for each layer, we choose  $K_1 = \dots = K_L = K = 64$  hidden nodes. Details of the other hyperparameters are described in the Supplementary Materials. Since the dimension of the input in our setting is small, usually only  $D = 2$  or  $3$ , while the effective sample size, i.e., the number of voxels, is sufficiently large, we have found that the results are not overly sensitive to the choice of  $L$  and  $K$ . (See Section 4.3 for details.)

## 3 Theory

In this section, we establish the theoretical properties of the proposed method. We first define the function class for the nonparametric functions in our model. We next present the set of regularity conditions, under which we derive the error bounds and establish the estimation and selection consistency.

### 3.1 Function class

As is common for any nonparametric theoretical analysis, we first explicitly define the class of candidate functions for our method. We follow the general framework of Bauer et al. (2019); Schmidt-Hieber et al. (2020), and begin with the definition of smooth generalized hierarchical interaction model. We then extend the notion to the concept of the *piecewise* smooth generalized hierarchical interaction model. Finally, we define the candidate neural network function class for our proposed method.

**Definition 1** (Hölder smoothness). For  $D \in \mathbb{N}_+$ ,  $C \in \mathbb{R}_+$ , and  $P = P' + P'' \in \mathbb{R}_+$ , where  $P' = \lceil P - 1 \rceil$ , i.e., the smallest integer no smaller than  $P - 1$ , a function  $f : \mathbb{R}^D \rightarrow \mathbb{R}$  is said to be smooth with Hölder index  $P$ , or simply  $P$ -smooth, if for every  $(p_1, \dots, p_D) \in \mathbb{N}_0^D$  with  $\sum_{d=1}^D p_d = P'$ , we have: (a) the partial derivative  $\{\partial^{P'} / (\partial d_1^{p_1} \dots \partial d_D^{p_D})\} f$  exists; (b) for any  $\mathbf{u} \in \mathbb{R}^D$ ,  $\{\partial^{P'} / (\partial u_1^{p_1} \dots \partial u_D^{p_D})\} f(\mathbf{u}) < C$ ; and (c) for all  $\mathbf{u}, \mathbf{u}' \in \mathbb{R}^D$ ,  $|\{\partial^{P'} / (\partial u_1^{p_1} \dots \partial u_D^{p_D})\} f(\mathbf{u}) - \{\partial^{P'} / (\partial u_1^{p_1} \dots \partial u_D^{p_D})\} f(\mathbf{u}')| \leq C \|\mathbf{u} - \mathbf{u}'\|_2^{P''}$ .

**Definition 2** (Smooth generalized hierarchical interaction model). For  $D, D', L', K' \in \mathbb{N}_+$  and  $P \in \mathbb{R}_+$ , a function  $f : \mathbb{R}^D \rightarrow \mathbb{R}$  is called a  $K'$ -component  $P$ -smooth generalized hierarchical interaction model of depth  $L'$  and order  $D'$ , if it satisfies:

- (a) When  $L' = 0$ , there exist  $\mathbf{a}_d \in \mathbb{R}^D$ ,  $d = 1, \dots, D'$ , and  $g : \mathbb{R}^{D'} \rightarrow \mathbb{R}$ , such that  $f(\mathbf{u}) = g(\mathbf{a}_1^\top \mathbf{u}, \dots, \mathbf{a}_{D'}^\top \mathbf{u})$ , where  $g$  is  $P$ -smooth, and  $K' = 1$ .
- (b) When  $L' > 0$ , there exist  $g_k : \mathbb{R}^{D'} \rightarrow \mathbb{R}$ , and  $h_{k,d} : \mathbb{R}^D \rightarrow \mathbb{R}$ , such that  $f(\mathbf{u}) = \sum_{k=1}^{K'} g_k(h_{k,1}(\mathbf{u}), \dots, h_{k,D'}(\mathbf{u}))$ , where  $g_k$  is  $P$ -smooth, and  $h_{k,d}$  is a  $K'$ -component  $P$ -smooth generalized hierarchical interaction model of depth  $L' - 1$  and order  $D'$ ,  $k = 1, \dots, K'$ ,  $d = 1, \dots, D'$ ,

Definition 1 gives a general definition of function smoothness, by bounding the derivatives up to a certain degree. Definition 2 describes a family of functions that are constructed by recursion and summation of multiple layers of Hölder-smooth functions defined in Definition 1, which covers a wide range of functions (Bauer et al., 2019).

Next, we generalize Definition 2, by allowing the functions to be *piecewise* smooth.

**Definition 3** (Piecewise smooth generalized hierarchical interaction model). For  $D, D', L', K', Q \in \mathbb{N}_+$  and  $P \in \mathbb{R}_+$ , a function  $f : \mathbb{R}^D \rightarrow \mathbb{R}$  is called a  $K'$ -component  $Q$ -sided piecewise  $P$ -smooth generalized hierarchical interaction model of depth  $L'$  and order  $D'$ , if it satisfies:

- (a) When  $L' = 0$ , there exist  $\mathbf{a}_d \in \mathbb{R}^D$ ,  $d = 1, \dots, D'$ ,  $g : \mathbb{R}^{D'} \rightarrow \mathbb{R}$ , and  $\Omega \subset \mathbb{R}^D$ , such that  $f(\mathbf{u}) = g(\mathbf{a}_1^\top \mathbf{u}, \dots, \mathbf{a}_{D'}^\top \mathbf{u}) \times \mathbb{I}_\Omega(\mathbf{u})$ , where  $g$  is  $P$ -smooth,  $\Omega$  is a  $Q$ -sided  $D$ -dimensional polytope, and  $K' = 1$ .
- (b) When  $L' > 0$ , there exist  $g_k : \mathbb{R}^{D'} \rightarrow \mathbb{R}$ ,  $h_{k,d} : \mathbb{R}^D \rightarrow \mathbb{R}$ , and  $\Omega_k \subset \mathbb{R}^D$ , such that  $f(\mathbf{u}) = \sum_{k=1}^{K'} g_k(h_{k,1}(\mathbf{u}), \dots, h_{k,D'}(\mathbf{u})) \times \mathbb{I}_{\Omega_k}(\mathbf{u})$ , where  $g_k$  is  $P$ -smooth and  $h_{k,d}$  is a  $K'$ -component  $P$ -smooth generalized hierarchical interaction model of depth  $L' - 1$  and order  $D'$ , and  $\Omega_k \subset \mathbb{R}^D$  is a  $Q$ -sided  $D$ -dimensional polytope,  $k = 1, \dots, K'$ ,  $d = 1, \dots, D'$ .

Definition 3 generalizes Definition 2, and describes a family of piecewise smooth functions. This family again covers a wide range of functions. For instance, when  $D = 2$ , the nonzero regions of  $\beta$  can be partitioned into a finite number of hexagons, and  $\beta$  is Lipschitz continuous inside each partition,  $\beta$  is a 6-sided-piecewise 1-smooth generalized hierarchical interaction model of depth 1 and order 2. When  $K = 1$  and  $\mathcal{S} \subset \Omega_1$ , the function is smooth over the entire spatial domain, and satisfies both Definition 2 and Definition 3.

Next, we formally characterize the class of candidate neural network functions. The feed-forward deep neural network model (2) we use falls in this class.

**Definition 4** (Candidate neural network model). Let  $\phi(u) = \{1 + \exp(u)^{-1}\}^{-1}$ . For  $D, D', L', K', Q, M \in \mathbb{N}_+$  and  $\gamma \in \mathbb{R}_+$ , define  $\mathcal{G}_{D,D',L',K',Q}^{M,\gamma}$  to be the collection of all functions  $g : \mathbb{R}^D \rightarrow \mathbb{R}$  that satisfy:

- (a) When  $L' = 0$ , there exist  $|\xi_{m,b,d}^{[1]}|, |\xi_{m,b}^{[2]}|, |\xi_m^{[3]}| \in (0, \gamma)$ ,  $m = 0, \dots, M, b = 0, \dots, 4D' + Q, d = 0, \dots, D$ , such that

$$g(\mathbf{u}) = \sum_{m=1}^M \xi_m^{[3]} \phi \left( \sum_{b=1}^{4D'+Q} \xi_{m,b}^{[2]} \phi \left( \sum_{d=1}^D \xi_{m,b,d}^{[1]} u_d + \xi_{m,b,0}^{[1]} \right) + \xi_{m,0}^{[2]} \right) + \xi_0^{[3]},$$

and  $K' = 1$ .

- (b) When  $L' > 0$ , there exist  $g_k \in \mathcal{G}_{D,D',0,K',Q}^{M,\gamma}$  and  $h_{k,b} \in \mathcal{G}_{D,D',L'-1,K',Q}^{M,\gamma}$ ,  $k = 1, \dots, K', b = 1, \dots, D'$ , such that  $g(\mathbf{u}) = \sum_{k=1}^{K'} g_k(h_{k,1}(\mathbf{u}), \dots, h_{k,D'}(\mathbf{u}))$ .

Definition 4 describes a family of neural network functions,  $\mathcal{G}_{D,D',L',K',Q}^{M,\gamma}$ , obtained from recursively composing and taking the sum of two-layer fully connected feed-forward neural networks. The recursion is repeated  $L'$  times. At each recursion, the output is the sum of  $K'$  two-layer fully connected feed forward neural networks, where each has  $M$  hidden nodes in the second hidden layer,  $4D' + Q$  hidden nodes in the first hidden layer, and  $D'$  nodes in the input layer. Moreover, we take the logistic function as the activation function  $\phi$  in Definition 4, following Bauer et al. (2019). Similar results can be obtained when using the ReLU activation function (Schmidt-Hieber et al., 2020).

We remark that, in our theoretical analysis, we study the family of piecewise smooth functions as described in Definition 3, which we assume  $\beta(\mathbf{s}), \alpha(\mathbf{s}), \sigma^2(\mathbf{s})$  all belong to. We then employ the candidate neural network functions as described in Definition 4 to approximate the true functions  $\beta(\mathbf{s}), \alpha(\mathbf{s}), \sigma^2(\mathbf{s})$ .

We also remark on the constants introduced in Definition 3 and Definition 4. In particular,  $P$  reflects the smoothness level of the functions that we study, and  $Q$  is the number of sides of the polytope that

characterizes the boundary of the piecewise functions. The constant  $D$  is the dimension of the observed image, and  $D'$  is the order of the generalized hierarchical interaction model. The constants  $L'$  and  $K'$  are the number of layers and the number of components in the recursive construction of the true functions and the candidate functions. The constant  $\gamma$  is the bound of the absolute values of the weight parameters in the neural network functions, and  $M$  corresponds to the number of hidden nodes in the recursive construction of the two-layer feed-forward neural networks. In our theoretical analysis, following Bauer et al. (2019); Schmidt-Hieber et al. (2020), we use the same  $L', K'$  for the true and candidate functions. We let  $M$  and  $\gamma$  control the complexity of the neural network model that we use, and allow  $M$  and  $\gamma$  to diverge along with the number of voxels  $V$  and the number of images  $N$ .

### 3.2 Regularity conditions

We first list a set of regularity conditions needed to establish the convergence rate of the estimation error of our method.

**Assumption 1.** For  $i = 1, \dots, N$  and  $j = 1, \dots, J$ , suppose the true functions  $\beta_j(\cdot)$ ,  $\alpha_i(\cdot)$ , and  $\sigma^2(\cdot)$  are  $K'$ -component  $Q$ -sided piecewise  $P$ -smooth generalized hierarchical interaction models of depth  $L'$  and order  $D'$ , with Hölder smoothness constant  $C$ . In addition, for the corresponding spatial domain  $\mathcal{S}$ , there exists a constant  $c_0 \in \mathbb{R}_+$ , such that  $\mathcal{S} \subset [-c_0, c_0]^D$ .

**Assumption 2.** The random covariates  $\mathbf{x}_1, \dots, \mathbf{x}_N$  are i.i.d., with  $\mathbb{E}[\mathbf{x}_1] = \mathbf{0}$ ,  $\mathbb{E}[\|\mathbf{x}_1\|_2^4] < c_1$ , and  $\|\text{Cov}(\mathbf{x}_1)\|_F^2 < c_2$  (where  $\|\cdot\|_F$  is the Frobenius norm). In addition, there exist constants  $c_3, c_4 \in \mathbb{R}_+$ , such that  $\mathbb{E}(\exp[c_3\{\mathbf{x}_1^\top \boldsymbol{\beta}(\mathbf{s}) + \epsilon(\mathbf{s})\}^2]) < c_4$ , for all  $\mathbf{s} \in \mathcal{S}$ .

Assumption 1 places smoothness requirements on the true functions, which is common in the varying coefficient model literature. For instance, Zhu et al. (2014) imposed smoothness by requiring the function to be piecewise Lipschitz continuous. Li et al. (2020) imposed smoothness by assuming the function to be in a Sobolev space. Moreover, we assume that the domain of those spatially varying functions is contained in a compact set, which is true in practice for most imaging studies, as the measurement boundary of the imaging machine is usually bounded. Assumption 2 places the bounds on the moments of the covariates.

**Assumption 3.** The neural network approximation functions belong to the class specified in Definition 4, i.e.,  $\mathcal{N}_{\beta_j}(\cdot | \boldsymbol{\theta}_{\beta_j}) \in \mathcal{G}_{D, D', L', K', Q}^{M, \gamma_\beta}$ ,  $\mathcal{N}_{\alpha_i}(\cdot | \boldsymbol{\theta}_{\alpha_i}) \in \mathcal{G}_{D, D', L', K', Q}^{M, \gamma_\alpha}$ , and  $\mathcal{N}_\sigma(\cdot | \boldsymbol{\theta}_\sigma) \in \mathcal{G}_{D, D', L', K', Q}^{M, \gamma_\sigma}$ , for  $i = 1, \dots, N$  and  $j = 1, \dots, J$ . Moreover,  $\gamma_\beta = (NV)^{c_5}$  and  $\gamma_\alpha = \gamma_\sigma = V^{c_6}$  for some constants  $c_5, c_6 \in \mathbb{R}_+$ . Furthermore, there exists a constant  $c_7 > 0$ , such that, for any  $\mathbf{s} \in \mathcal{S}$ ,  $\|\mathcal{N}(\mathbf{s} | \hat{\boldsymbol{\theta}}_\beta)\|_2^2 < c_7 \log(NV)$ ,  $\|\mathcal{N}(\mathbf{s} | \hat{\boldsymbol{\theta}}_\alpha)\|_2^2 < c_7 \log(V)$ , and  $\mathcal{N}(\mathbf{s} | \hat{\boldsymbol{\theta}}_\sigma)^2 < c_7 \log(V)$ .

**Assumption 4.** There exists a constant  $c_8 > 0$  independent of  $N$ , such that the  $L_1$  penalty parameter  $\lambda$  in (4) satisfies  $\lambda \leq c_8 V^{-1}$ .

Assumption 3 specifies the candidate neural network functions that we use to approximate the true functions in the varying coefficient model. Moreover, it bounds the absolute values of the weight parameters in the neural network functions  $\gamma$ , as well as the  $L_2$  norm of the neural network estimators. Assumption 4 places a rate requirement on the  $L_1$  regularization parameter  $\lambda$  in (4). Similar requirements on the  $L_1$  penalty have been imposed in the studies of sign consistency of LASSO-based selection. For example, in Zhao and Yu (2006), the rate of the penalty weight is set to be strictly between  $\mathcal{O}(1)$  and  $\mathcal{O}(n^{-\frac{1}{2}})$ . In comparison, the estimator in (4) is penalized with a lighter weight, since we further apply hard thresholding afterwards in (5).

We next list two additional regularity conditions needed to establish the convergence rate of the selection error of our method.

**Assumption 5.** There exists a constant  $c_9 \in \mathbb{R}_+$ , such that  $\inf_{\beta_j(\mathbf{s}) \neq 0} |\beta_j(\mathbf{s})| > c_9$ , and  $\mu(\{\mathbf{s} \in \mathcal{S} : \beta_j(\mathbf{s}) \neq 0\}) / \mu(\mathcal{S}) \ll 1$ , for  $j = 1, \dots, J$ , where  $\mu$  is a Lebesgue measure of the size of a set in the spatial domain  $\mathcal{S} \subset \mathbb{R}^D$ .

**Assumption 6.** There exists a constant  $c_{10} \in \mathbb{R}_+$ , such that  $\eta_j \rightarrow 0$  as  $M \rightarrow \infty$ , and  $\eta_j > c_{10} \log(M)^{-1}$ , for  $j = 1, \dots, J$ .

Assumption 5 requires that the main effects are sparse, and that there is a gap between zero and the weakest signal level. Assumption 6 requires the hard thresholding level  $\eta_j$  in (5) to converge to zero, but

at a rate not decaying too fast. In practice, this condition can be achieved by setting a minimum on the thresholding level.

### 3.3 Error bounds and consistency

In our theoretical analysis, we first establish in Theorem 1 the error bound of the estimator  $\tilde{\beta}(\mathbf{s})$  from (4), i.e., the estimator before the hard thresholding step (5). We next establish in Theorem 2 the error bound of the estimator  $\hat{\beta}(\mathbf{s})$  from (5) after hard thresholding. We then obtain in Corollary 3 the error bound of the estimators  $\hat{\alpha}(\mathbf{s})$  from (6) and  $\hat{\sigma}^2(\mathbf{s})$  from (7). Finally, in Corollaries 4 and 5, we express the error bounds when the neural network complexity is a function of the number of voxels and images.

We first derive the error bound, in terms of the  $L_2$  estimation error, of the estimator  $\tilde{\beta}(\mathbf{s})$  of the main effect function  $\beta$  before applying hard thresholding. Recall that  $D$  is the dimension of the observed image,  $P$  reflects the degree of smoothness of the true function  $\beta$ , and  $M$  is associated with the total number of nodes and thus reflects the complexity of the neural network functions.

**Theorem 1.** *There exists a constant  $c_{11} \in \mathbb{R}_+$  that, for sufficiently large  $N$  and  $V$ ,*

$$\mathbb{E} \left\{ \frac{1}{V} \sum_{v=1}^V \left\| \tilde{\beta}(\mathbf{s}_v) - \beta(\mathbf{s}_v) \right\|_2^2 \right\} \leq c_{11} \left\{ \log(NV)^3 \left( \frac{M}{NV} + M^{-\frac{2P}{D}} \right) + \frac{1}{N} \right\}.$$

Theorem 1 decomposes the mean squared error of  $\tilde{\beta}(\mathbf{s})$  into the sum of three terms. The first term corresponds to the estimation error, i.e., the ‘‘variance’’ of the estimator. It decreases as the number of subjects  $N$  or the number of voxels  $V$  increases, i.e., when more data information becomes available, and it increases as the number of nodes in the neural network increases, since the candidate models become more flexible but also more variable. The second term corresponds to the approximation error, i.e., the ‘‘bias’’ for the estimator, that is related to the approximation capability of the neural network. This bias decreases as the neural network involves a larger number of nodes. The third term corresponds to the deviation from the true main effect induced by the error in estimating the individual deviation. Since the individual deviation is also spatially correlated, the error cannot be reduced simply by increasing the number of voxels, nor increasing the complexity of the neural network.

Next, we derive the error bound, in terms of both the  $L_2$  estimation error and the  $L_0$  sign error, of the estimator  $\hat{\beta}(\mathbf{s})$  of the main effect function  $\beta$  after applying hard thresholding. The result is built upon Theorem 1 and Markov’s inequality.

**Theorem 2.** *There exist constants  $c_{12}, c_{13} \in \mathbb{R}_+$  that, for sufficiently large  $N$  and  $V$ ,*

(a) *for the  $L_2$  estimation error,*

$$\mathbb{E} \left\{ \frac{1}{V} \sum_{v=1}^V \left\| \hat{\beta}(\mathbf{s}_v) - \beta(\mathbf{s}_v) \right\|_2^2 \right\} \leq c_{12} \left\{ \log(NV)^5 \left( \frac{M}{NV} + M^{-\frac{2P}{D}} \right) + \frac{\log(N)^2}{N} \right\};$$

(b) *for the  $L_0$  sign error,*

$$\mathbb{E} \left[ \frac{1}{V} \sum_{v=1}^V \left\| \text{sign} \{ \hat{\beta}(\mathbf{s}_v) \} - \text{sign} \{ \beta(\mathbf{s}_v) \} \right\|_0 \right] \leq c_{13} \left\{ \log(NV)^5 \left( \frac{M}{NV} + M^{-\frac{2P}{D}} \right) + \frac{\log(N)^2}{N} \right\}.$$

Theorem 2 obtains an  $L_2$  estimation error bound for  $\hat{\beta}(\mathbf{s})$  that is the same as that of  $\tilde{\beta}(\mathbf{s})$  in Theorem 1, up to a logarithmic factor. It implies that  $\hat{\beta}(\mathbf{s})$  is a consistent estimator of  $\beta(\mathbf{s})$ . Moreover, the  $L_0$  sign error bound is a weighted average between the false positive rate, the false negative rate, and the false sign flipping rate, where the weights depend on the true proportion of the three signs in the main effect function. This  $L_0$  sign error bound implies the region selection consistency. That is, let  $\mathcal{R}_j = \{ \mathbf{s}_v : \beta_j(\mathbf{s}_v) \neq 0, v = 1, \dots, V \}$  represent the true activation region for covariate  $j$ , and  $\hat{\mathcal{R}}_j = \{ \mathbf{s}_v : \hat{\beta}_j(\mathbf{s}_v) \neq 0, v = 1, \dots, V \}$  an estimate of  $\mathcal{R}_j$ . Then  $\hat{\mathcal{R}}_j$  converges to  $\mathcal{R}_j$  with probability one. To obtain both the estimation and selection consistency, we need the number of images  $N$  to go to infinity, with  $M$  increasing at a rate slower than  $\mathcal{O}(NV)$ , while the number of voxels  $V$  can be either fixed or diverge to infinity. (See Corollary 4 and Corollary 5 below for a detailed discussion of the relations between  $M$ ,  $N$ , and  $V$  that achieve the best convergence rate.)

Next, we derive the error bound, in terms of the  $L_2$  estimation error, of the estimators  $\hat{\alpha}(\mathbf{s})$  and  $\hat{\sigma}^2(\mathbf{s})$  of the individual deviation function  $\alpha(\mathbf{s})$  and the error variance  $\sigma^2(\mathbf{s})$ .

**Corollary 3.** *There exist constants  $c_{14}, c_{15} \in \mathbb{R}_+$  that, for sufficiently large  $N$  and  $V$ ,*

(a) *for the  $L_2$  estimation error of the individual deviation function estimator,*

$$\mathbb{E} \left\{ \frac{1}{NV} \sum_{v=1}^V \|\hat{\alpha}(\mathbf{s}_v) - \alpha(\mathbf{s}_v)\|_2^2 \right\} \leq c_{14} \left\{ \log(NV)^5 \left( \frac{M}{NV} + M^{-\frac{2P}{D}} \right) + \frac{\log(N)^2}{N} + \frac{\log(V)^3 M}{V} \right\}.$$

(b) *for the  $L_2$  estimation error of the error variance function estimator,*

$$\mathbb{E} \left\{ \frac{1}{V} \sum_{v=1}^V \|\hat{\sigma}^2(\mathbf{s}_v) - \sigma^2(\mathbf{s}_v)\|_2^2 \right\} \leq c_{15} \left\{ \log(NV)^5 \left( \frac{M}{NV} + M^{-\frac{2P}{D}} \right) + \frac{\log(N)^2}{N} + \frac{\log(V)^3 M}{V} \right\}.$$

Corollary 3 shows the error bounds of  $\hat{\alpha}(\mathbf{s})$  and  $\hat{\sigma}^2(\mathbf{s})$  converge to zero when both the number of images  $N$  and the number of voxels  $V$  approach infinity. This is slightly different from the error bound convergence of  $\hat{\beta}(\mathbf{s})$  as shown in Theorem 1, where only  $N$  is required to go to infinity, since when the number of images increases, the number of individual deviation functions to be estimated also increases. As such, a sufficient number of voxels is needed for estimating the individual deviations accurately. The same is true for estimating the error variance function.

In Theorems 1 and 2, the error bounds of  $\hat{\beta}(\mathbf{s})$  are functions of the number of images  $N$ , the number of voxels  $V$ , and the neural network complexity measure  $M$ . Next, we re-express the error bounds, first as functions of  $N$  and  $V$ , then as functions of  $V$  only.

**Corollary 4.** *Suppose  $M = c_{16}(NV)^{\frac{D}{D+2P}}$  for some constant  $c_{16} \in \mathbb{R}_+$ . Then there exist constants  $c_{17}, c_{18} \in \mathbb{R}_+$  that, for sufficiently large  $N$  and  $V$ ,*

(a) *for the  $L_2$  estimation error,*

$$\mathbb{E} \left\{ \frac{1}{V} \sum_{v=1}^V \|\hat{\beta}(\mathbf{s}_v) - \beta(\mathbf{s}_v)\|_2^2 \right\} \leq c_{17} \left\{ \log(NV)^5 (NV)^{-\frac{2P}{2P+D}} + \log(N)^2 N^{-1} \right\};$$

(b) *for the  $L_0$  sign error,*

$$\mathbb{E} \left[ \frac{1}{V} \sum_{v=1}^V \left\| \text{sign} \{ \hat{\beta}(\mathbf{s}_v) \} - \text{sign} \{ \beta(\mathbf{s}_v) \} \right\|_0 \right] \leq c_{18} \left\{ \log(NV)^5 (NV)^{-\frac{2P}{2P+D}} + \log(N)^2 N^{-1} \right\}.$$

Corollary 4 follows directly from Theorem 2, by setting the neural network complexity  $M$  proportional to  $(NV)^{D/(D+2P)} = (NV)^{1/(1+2P/D)}$ . The exponent  $1/(1+2P/D)$  controls the rate at which  $M$  needs to grow as  $N$  and  $V$  grow, and this exponent goes to zero as  $2P/D$  goes to infinity. Intuitively, when the true function  $\beta(\mathbf{s}_v)$  is highly smooth, i.e., when  $2P/D$  is large, a simple model is sufficient to approximate the true function well, and an overly complex model is more likely to induce overfitting. On the other hand, when the true function is highly non-smooth, i.e., when  $2P/D$  is small, a more complex model is needed to ensure an accurate approximation.

**Corollary 5.** *Suppose  $N = c_{19}V^{\frac{2P}{D}}$  for some constant  $c_{19} \in \mathbb{R}_+$ . Then there exist constants  $c_{20}, c_{21} \in \mathbb{R}_+$  that, for sufficiently large  $V$ ,*

(a) *for the  $L_2$  estimation error,*

$$\mathbb{E} \left\{ V^{-1} \sum_{v=1}^V \|\hat{\beta}(\mathbf{s}_v) - \beta(\mathbf{s}_v)\|_2^2 \right\} \leq c_{20} \log(V)^5 V^{-\frac{2P}{D}};$$

(b) *for the  $L_0$  sign error,*

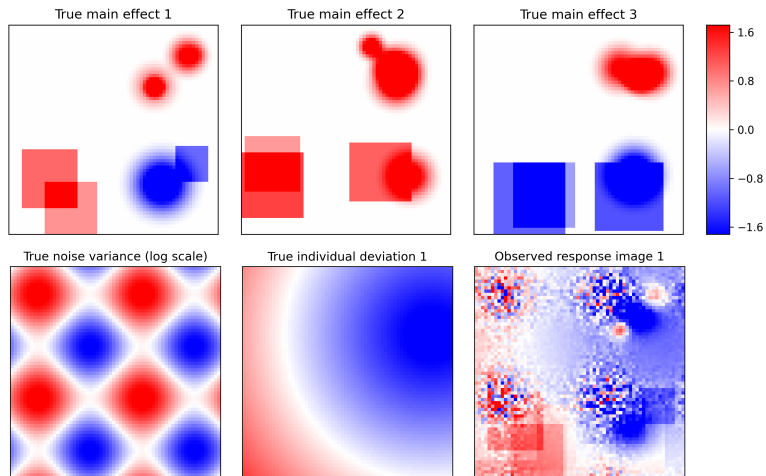
$$\mathbb{E} \left[ \frac{1}{V} \sum_{v=1}^V \left\| \text{sign} \{ \hat{\beta}(\mathbf{s}_v) \} - \text{sign} \{ \beta(\mathbf{s}_v) \} \right\|_0 \right] \leq c_{21} \log(V)^5 V^{-\frac{2P}{D}}.$$

Corollary 5 further simplifies the rate in Corollary 4, by expressing the number of images  $N$  as a function of the number of voxels  $V$ , where  $N$  is proportional to  $V^{-\frac{2P}{D}}$ , to achieve the best error bound in our setting. We note that our error bound is comparable to the minimax error bound  $N^{-\frac{2P}{2P+D}}$  in the classical nonparametric regression setting (Stone, 1982).

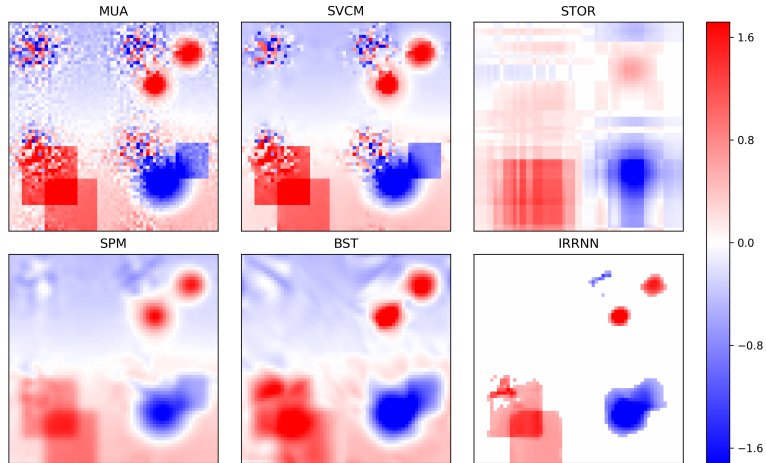
## 4 Simulations

In this section, we first lay out the setup of our simulation experiments. We then present the empirical performance of our proposed method, and compare it to some alternative solutions. We also carry out a sensitivity analysis to evaluate the robustness of our method with respect to the architecture of the deep neural network.

Figure 2: Image slices of the spatially varying functions of the true main effect, noise variance, an individual deviation, and a response image, along with the estimated main effects by various methods.



(a) True spatially varying coefficient functions and a response image.



(b) Estimated spatially varying coefficient functions by various methods.

### 4.1 Experimental setup

We generate the data following model (1), with  $J = 3$  covariates  $\mathbf{x}_i = (x_{i1}, \dots, x_{iJ})^\top$ ,  $i = 1, \dots, N$ , independently drawn from a standard normal distribution. We consider two sample sizes,  $N = 20$  and 50. We consider  $D = 3$ -dimensional images, with four image sizes,  $16 \times 16 \times 8$ ,  $32 \times 32 \times 8$ ,  $64 \times 64 \times 8$ , and  $128 \times 128 \times 8$ , resulting in  $V = 2,048$ , 8,192, 32,768, and 131,072 voxels, respectively. We generate the main effect function  $\beta_j(\mathbf{s})$ ,  $j = 1, \dots, J$ , the individual deviation function  $\alpha_i(\mathbf{s})$ ,  $i = 1, \dots, N$ , and the

error variance function  $\sigma^2(\mathbf{s})$  from a bounded 3-dimensional rectangular spatial domain  $\mathcal{S}$ . We consider different spatial patterns, as illustrated in Figure 2a.

More specifically, for  $\beta_j(\mathbf{s})$ , we divide the rectangular domain into four blocks, along the first two axes, and consider different spatial patterns in each of the four blocks. For the top-left block, we set the value of the spatially varying function to zero, so this region contains no signal. For the top-right block, we generate two spherical regions that contain signals with strength smoothly diminishing to zero at the boundary. The size and location of the two spherical regions are randomly and independently selected, and the two regions may be mutually exclusive or overlapping. If there is an overlap, the values inside the overlapping region are simply the sum of the values of the two individual regions. For the bottom-left block, we generate two rectangular regions with a constant signal level, resulting in sharp rather than smooth edges. For the bottom-right block, we generate a spatial pattern by mixing those in the top-right block and the bottom-left block. Figure 2a top row shows one realization of the generated main effect function.

For  $\alpha_i(\mathbf{s})$ , we first randomly select a spatial location as the center and assign a random signal value. We then proportionally increase or decrease the signal value according to the distance to the center. Figure 2a bottom left panel shows one realization of the generated individual deviation function.

For  $\sigma^2(\mathbf{s})$ , we generate the noise variance in a periodic manner across the three axes by using a random linearly transformed sine function. Figure 2a bottom center panel shows one realization of the generated error variance function. Given the variance, we generate the measurement error from two distributions, a standard normal and a  $(\chi_3^2 - 3)/\sqrt{6}$  distribution.

In our simulations, we consider the setting where the signal strength is relatively low, by choosing the ratio of the variances of the main effect, the individual deviation, and the error to 0.2 : 0.5 : 1.0. This mimics the highly noisy imaging data setting that is often the rule rather than the exception in biomedical imaging studies. Figure 2a bottom right panel shows a two-dimensional slice of a realization of the generated response image.

## 4.2 Empirical estimation and selection accuracy

We compare our method with a number of alternative solutions. These include the massive univariate analysis (MUA), and the massive univariate analysis after pre-smoothing (SPM), in combination with random field theory for selection, which is implemented in the neuroimaging software SPM (Friston, 2003). Both of these methods are frequently used in the neuroscience community. We also compare our method with the sparse tensor response regression (STOR) of Sun and Li (2017), the spatially varying coefficient model with jump discontinuities (SVCM) of Zhu et al. (2014), and the bivariate splines over triangulation-based spatially varying coefficient model (BST) of Li et al. (2020). (Since BST is designed for two-dimensional images, we apply it to slices of the three-dimensional image and then stack the two-dimensional estimates). We name our method as image response regression via neural networks (IRRNN). We evaluate and compare the methods in terms of estimation and selection accuracy. For the estimation accuracy, we report the mean squared error (MSE) between the estimated and the true function. For the selection accuracy, we report the area under the operating characteristic curve (AUC), the false positive error rate (FPR), and the true positive rate (TPR). We repeat each simulation 50 times, and report the median and interquartile range of various criteria across 50 data replications. We have chosen the median because some of the alternative methods can produce unstable estimates. Table 1 reports the empirical MSE, AUC, FPR and TPR.

For the estimation accuracy, our proposed method achieves uniformly the smallest MSE. We make a few additional observations. The advantage of IRRNN is more prominent when the imaging resolution is high. There is a clear trend of decreasing MSE for IRRNN when the number of voxels  $V$  increases. This agrees with our expectation, as we turn  $V$  as our effective sample size. Moreover, the improvement of IRRNN is more prominent when the number of images  $N$  is small than when  $N$  is large. This demonstrates the advantage of our method for medical imaging studies with a limited sample size. Finally, our method is robust against a skewed error distribution. In contrast, the alternative methods of SPM, BST and STOR, when the number of images is small, show a clear increase of MSE as the error becomes a chi-squared distribution.

For selection accuracy, our proposed method achieves the highest AUC, except for when  $N$  and  $V$  are both the smallest, in which case our AUC is still comparable to the alternative methods. Meanwhile,

Table 1: The estimation and selection accuracy of various methods. The number of images is  $N = 20, 50$ . The image dimension is  $R \times R \times 8$ , with  $R = 16, 32, 64, 128$ . The reported numbers are in 0.01 units.

$M$	$R$	$\mathcal{N}(0, 1)$ noise						$(\chi_3^2 - 3)/\sqrt{6}$ noise					
		MUA	SPM	BST	STOR	SVCM	IRRNN	MUA	SPM	BST	STOR	SVCM	IRRNN
Mean squared error (MSE)													
20	16	191 (57)	61 (32)	63 (31)	63 (27)	157 (51)	38 (22)	187 (78)	66 (41)	69 (43)	59 (36)	153 (73)	35 (19)
20	32	190 (59)	59 (36)	59 (34)	51 (33)	161 (53)	28 (15)	185 (64)	63 (41)	64 (41)	52 (31)	155 (64)	25 (18)
20	64	192 (58)	58 (37)	58 (35)	47 (32)	160 (50)	23 (19)	185 (66)	62 (41)	62 (42)	53 (31)	158 (64)	20 (18)
20	128	193 (54)	58 (37)	56 (36)	44 (31)	161 (50)	22 (16)	186 (64)	62 (41)	61 (42)	50 (30)	157 (63)	19 (19)
50	16	66 (12)	30 (10)	27 (11)	28 (10)	52 (12)	25 (08)	65 (16)	32 (14)	26 (14)	30 (10)	51 (15)	24 (11)
50	32	65 (11)	26 (11)	24 (11)	24 (08)	52 (10)	16 (08)	66 (17)	27 (13)	24 (13)	26 (09)	52 (14)	15 (10)
50	64	65 (10)	24 (11)	22 (11)	23 (10)	52 (11)	12 (07)	66 (16)	25 (13)	22 (13)	22 (11)	53 (14)	13 (08)
50	128	64 (10)	24 (10)	21 (10)	22 (08)	51 (11)	11 (06)	67 (15)	24 (14)	21 (14)	21 (09)	53 (13)	11 (08)
Area under the operating characteristic curve (AUC)													
20	16	66 (08)	63 (13)	64 (11)	61 (12)	67 (09)	65 (10)	68 (07)	64 (12)	66 (08)	62 (14)	67 (08)	64 (10)
20	32	66 (08)	66 (11)	66 (11)	64 (15)	67 (10)	69 (08)	67 (07)	67 (10)	68 (07)	64 (12)	67 (08)	70 (10)
20	64	66 (07)	67 (11)	67 (10)	65 (12)	67 (09)	70 (06)	67 (07)	68 (10)	69 (07)	66 (09)	68 (08)	71 (09)
20	128	66 (08)	67 (11)	68 (11)	64 (09)	67 (09)	70 (06)	67 (07)	68 (10)	69 (07)	64 (11)	68 (08)	71 (09)
50	16	76 (08)	74 (11)	77 (09)	74 (14)	77 (08)	78 (09)	75 (07)	74 (12)	76 (08)	73 (09)	77 (08)	78 (09)
50	32	76 (08)	77 (10)	78 (09)	77 (14)	77 (08)	81 (06)	75 (07)	77 (10)	77 (09)	73 (10)	76 (08)	79 (08)
50	64	76 (08)	78 (09)	79 (09)	76 (16)	78 (08)	81 (05)	75 (06)	78 (09)	78 (08)	75 (09)	77 (07)	80 (08)
50	128	76 (08)	79 (08)	79 (09)	76 (15)	78 (08)	81 (06)	75 (07)	78 (09)	78 (09)	74 (12)	77 (07)	81 (08)
False positive rate (FPR)													
20	16	04 (05)	00 (00)	23 (20)	45 (53)	08 (06)	05 (04)	04 (04)	00 (00)	23 (14)	51 (59)	07 (04)	04 (04)
20	32	04 (05)	00 (00)	23 (21)	80 (85)	08 (06)	04 (04)	03 (04)	00 (00)	23 (14)	75 (79)	07 (04)	03 (04)
20	64	04 (05)	00 (00)	23 (21)	82 (76)	08 (07)	03 (04)	03 (04)	00 (00)	24 (15)	85 (61)	08 (04)	03 (04)
20	128	04 (05)	00 (00)	23 (22)	89 (81)	08 (07)	03 (04)	03 (04)	00 (00)	24 (15)	84 (75)	08 (05)	03 (04)
50	16	04 (04)	00 (00)	38 (14)	41 (47)	07 (06)	05 (04)	05 (05)	00 (00)	41 (20)	56 (52)	08 (06)	05 (03)
50	32	03 (05)	00 (00)	39 (15)	86 (79)	08 (06)	03 (04)	04 (05)	00 (00)	42 (19)	63 (72)	08 (06)	04 (04)
50	64	03 (05)	00 (00)	39 (15)	85 (82)	07 (06)	03 (04)	04 (05)	00 (00)	42 (19)	90 (63)	08 (06)	04 (03)
50	128	04 (05)	00 (00)	39 (14)	69 (82)	07 (06)	03 (04)	04 (05)	00 (00)	43 (19)	79 (74)	08 (06)	03 (04)
True positive rate (TPR)													
20	16	21 (08)	00 (01)	45 (20)	69 (54)	28 (11)	19 (09)	23 (09)	00 (01)	45 (18)	71 (59)	29 (12)	21 (10)
20	32	22 (07)	01 (02)	47 (16)	85 (75)	27 (10)	24 (09)	24 (09)	01 (02)	49 (16)	81 (65)	29 (14)	25 (10)
20	64	22 (07)	01 (01)	48 (15)	91 (36)	28 (10)	25 (07)	23 (08)	01 (02)	51 (14)	95 (33)	30 (13)	26 (10)
20	128	22 (07)	01 (01)	49 (16)	93 (55)	28 (10)	25 (07)	24 (09)	01 (01)	52 (16)	92 (47)	30 (13)	26 (10)
50	16	42 (09)	02 (03)	73 (09)	79 (43)	49 (11)	36 (11)	43 (07)	03 (03)	73 (10)	82 (28)	50 (07)	39 (10)
50	32	42 (10)	05 (04)	75 (10)	97 (39)	41 (12)	42 (09)	43 (08)	05 (04)	75 (10)	89 (28)	50 (09)	44 (09)
50	64	42 (10)	05 (03)	76 (10)	97 (44)	50 (11)	43 (09)	43 (08)	06 (04)	76 (10)	97 (23)	51 (09)	45 (09)
50	128	42 (10)	04 (03)	78 (09)	94 (46)	50 (11)	45 (09)	43 (08)	05 (03)	77 (10)	95 (36)	51 (09)	46 (09)

our method achieves the best overall performance in terms of FPR and TPR. SVCM, BST, and STOR tend to be overly liberal in selection, while SPM tend to be excessively conservative. MUA has the best selection balance among the alternative methods, but in comparison, as  $V$  increases, IRRNN achieves higher TPR, without losing control over the FNR. In addition, the performance of IRRNN is robust for both the Gaussian and the chi-squared error distributions.

Figure 2b shows the estimated main effect function for one data replication by various estimation methods, for  $N = 20$  images of dimension  $64 \times 64 \times 8$  with a Gaussian error. MUA produces the most noisy estimate, which is expected as it ignores the spatial information. Its estimation accuracy on an individual voxel highly depends on its local noise level, as shown by the contrast of the estimates in the noisy regions versus the other regions. Next, SVCM, which is based on smoothing the noise in the MUA estimates, eliminates the majority of the estimation errors in the low-noise regions, but most of the fluctuations in the high-noise regions have remained. In contrast, SPM and BST are less susceptible to white noise, but they tend to generate errors of wrinkled patterns, ignore the bias from the gradual transition in the background, and over-smooth the true signals, as shown in the blurry boundaries of the rectangular activation regions in the estimates. Moreover, STOR favors activation regions with rectangular boundaries, due to its treatment of images as low-rank tensors, but it tends to overlook the activation regions with curvy boundaries. Finally, IRRNN successfully detects all the activation regions of various geometric shapes, with the ability to adapt for both smooth and sharp boundaries. It also eliminates most of the noise and generates the cleanest estimate. In summary, IRRNN achieves the most competitive performance compared to the alternative methods, all under a rather limited sample size with a relatively large amount of noise in the data.

### 4.3 Sensitivity analysis

To assess the robustness of our method with respect to the architecture of the neural network, we repeat the previous experiments by using network architectures with various depths and widths, from 2 layers  $\times$  16 nodes per layer to 7 layers  $\times$  512 nodes per layer. After replicating the experiment on each architecture for 50 times, the median and IQR of the estimation MSE are reported in the Supplementary Materials. Estimation accuracy of IRRNN varies little across different DNN architectures when each layer contains at least 64 nodes. Although the MSE becomes higher when the number of nodes per layer is reduced to 32 or less, our method is still substantially more accurate and more stable than the alternative methods. This result shows that our model is relatively robust against the complexity of the neural networks.

## 5 Brain Imaging Applications

In this section, we illustrate our method with two neuroimaging applications, the Autism Brain Imaging Data Exchange (ABIDE) study, and the Adolescent Brain Cognitive Development (ABCD) study. Both studies have collected fMRI images from multiple imaging sites, along with clinical and demographic information. We investigate the association between cognitive ability and imaging response, which corresponds to the degree of inter-brain connectedness in ABIDE and brain activity when engaging working memory in ABCD.

### 5.1 ABIDE study

The overarching goal of the ABIDE study is to improve the neurological understanding of autism and its associated cognitive behaviors (Di Martino et al., 2014). In our data analysis, we use the Phase I data that consists of fMRI images from 19 imaging sites. The imaging data are preprocessed with the usual pipeline of Craddock et al. (2013); He et al. (2019). The response image is the weighted degrees of network connectivity, which measure each voxel’s number of direct connections to other voxels. The resulting imaging dimension is  $61 \times 73 \times 61$ . The  $J = 4$  covariates include cognitive ability, autism status, age, and sex. After removing the missing values, the number of subjects is  $N = 821$ . We apply IRRNN and compare it with MUA, SPM, and SVCM. We are unable to evaluate STOR and BST, as their official software programs report error messages when analyzing this particular dataset.

We first evaluate the estimation accuracy, by reporting the cross-validation of the mean squared error of the recovered response image. That is, we apply the methods to the data from one imaging site, then evaluate them on the data from all other imaging sites. Table 2 reports the cross-site testing MSE. We sort the experiments by the performance of MUA, which reflects the baseline difficulty of each estimation task. In the majority of the analyses, our method has the best estimation accuracy. In particular, when the estimation task is relatively easy, as indicated by the smaller MSE by MUA, all methods have similar performance. However, as difficulty increases, the differences between the methods are widened, and IRRNN become consistently more accurate than the alternative methods.

We next evaluate the selection accuracy. Again, since the true parameter functions are unknown for the real data, we evaluate the methods by their reproducibility in selecting important voxels. That is, we first obtain the set of selected voxels from the analysis of the data combined from all imaging sites. We then identify the set of selected voxels from the analysis of each individual imaging site. We claim a selected voxel from the all-site analysis is reproducible if it is selected in at least five single-site analyses. Table 3 reports the proportion of the reproducible voxels by all the methods. Our method achieves the highest proportion of reproducible voxels, which doubles that of SVCM, while the reproducible proportion for MUA and SPM are almost zero. The selection reproducibility is visualized in Figure 3a.

Table 2: Cross-site testing MSE for recovering imaging response in the brain fMRI studies. Each row represents a single-site analysis, where the data from one study site is used for training and those from the other sites are used for testing.

(a) ABIDE				(b) ABCD			
MUA	SPM	SVCM	IRRNN	MUA	SPM	SVCM	IRRNN
1.54	1.46	1.50	<b>1.43</b>	2.74	2.71	2.72	<b>2.69</b>
1.62	1.80	<b>1.59</b>	1.65	2.76	2.72	2.72	<b>2.68</b>
1.69	<b>1.47</b>	1.68	1.63	2.83	2.81	2.80	<b>2.78</b>
1.79	1.98	1.77	<b>1.76</b>	2.84	2.79	2.80	<b>2.74</b>
1.80	<b>1.53</b>	1.75	1.65	2.85	2.79	2.81	<b>2.75</b>
1.83	<b>1.53</b>	1.79	1.68	2.85	2.80	2.81	<b>2.74</b>
1.83	<b>1.59</b>	1.74	1.68	2.86	2.79	2.82	<b>2.73</b>
<b>1.91</b>	2.18	1.91	1.98	2.93	<b>2.88</b>	2.91	2.89
1.96	2.07	1.92	<b>1.84</b>	2.97	2.89	2.91	<b>2.76</b>
<b>1.98</b>	2.27	1.98	2.00	3.07	<b>2.92</b>	3.02	2.97
2.02	2.06	1.92	<b>1.76</b>	3.09	2.95	2.98	<b>2.83</b>
2.47	2.29	2.25	<b>1.76</b>	3.44	3.38	3.39	<b>3.31</b>
<b>2.62</b>	2.89	2.62	2.69	3.47	3.50	<b>3.47</b>	3.50
3.26	2.39	2.80	<b>2.19</b>	3.50	3.50	3.48	<b>3.42</b>
3.61	2.79	3.21	<b>1.74</b>	3.53	3.52	<b>3.51</b>	3.54
5.18	3.76	4.99	<b>3.65</b>	3.71	3.61	3.63	<b>3.58</b>
6.00	3.58	-	<b>3.03</b>	4.30	3.66	3.85	<b>3.02</b>
6.61	4.41	5.93	<b>3.28</b>	5.82	4.87	5.24	<b>4.01</b>
7.33	5.25	7.05	<b>5.41</b>	7.28	5.58	6.34	<b>3.63</b>
				113.28	73.12	113.28	<b>4.16</b>

Table 3: Selection consistency in the brain fMRI studies, as measured by the proportion of voxels selected in the all-site analysis that are also consistently selected in single-site analyses.

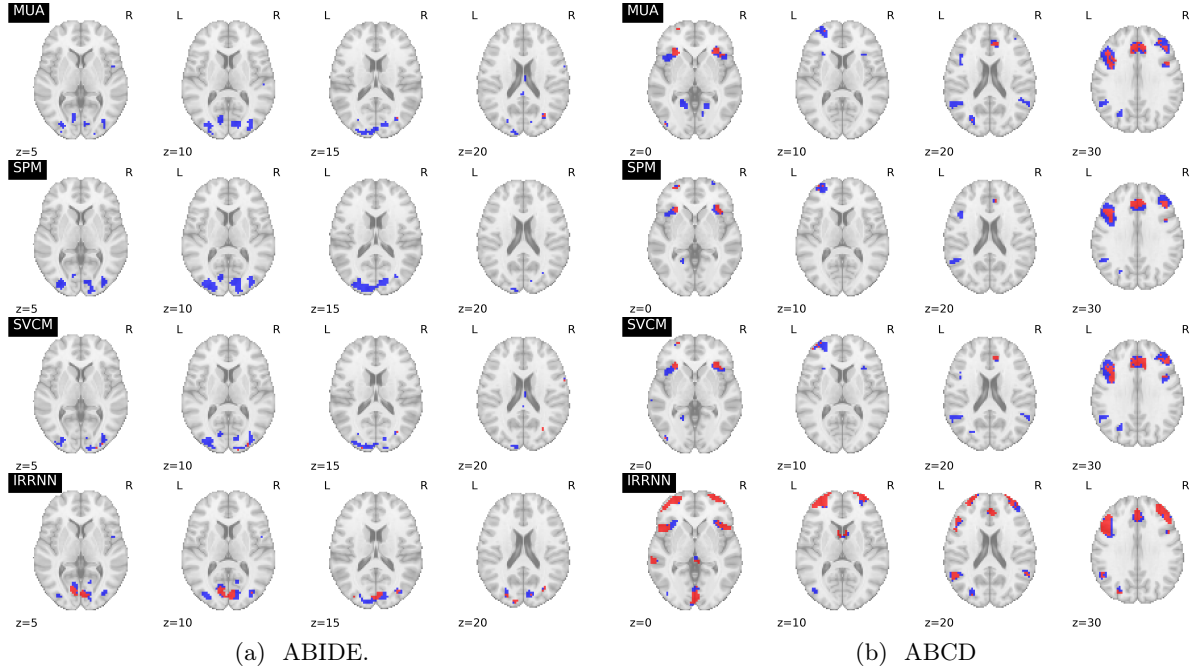
Study	MUA	SPM	SVCM	IRRNN
ABIDE	0.021	0.000	0.168	0.365
ABCD	0.397	0.423	0.428	0.655

We also present a summary of the selected voxels from all imaging sites. We first map those voxels to a set of predefined brain anatomical regions following the widely used automated anatomical labeling (AAL) atlas (Tzourio-Mazoyer et al., 2002). Then we further group these regions into a set of functional networks (Power et al., 2011). Table 4 reports the top selected regions and functional networks. These findings are consistent with the literature on cognitive ability. In particular, we have selected a high proportion of voxels in the regions of occipital lobe (Goriounova and Mansvelder, 2019; Yoon et al., 2017; Simard et al., 2015; Menary et al., 2013), the calcarine fissure and surrounding cortex (Yu et al., 2008), and the cuneus (Schnack et al., 2015; Haier et al., 2004; Song et al., 2008). In addition, these regions all belong to the visual functional network, which has been found to be closely related to cognitive ability (Dubois et al., 2018; Hearne et al., 2016). Compared to the alternative methods, IRRNN’s reproducibility is higher in most of the top regions and functional networks. This result shows the selection consistency of IRRNN inside biologically meaningful imaging regions.

## 5.2 ABCD study

The ABCD study aims at delineating the associations between cognitive behaviors and brain development (Casey et al., 2018). In our analysis, we use the annual release 1.1 that consists of minimally preprocessed two-back task-based fMRI data from 20 imaging sites (Hagler Jr et al., 2019). The response image we analyze is the contrast map of the two-back task, which has been consistently found to engage brain regions for memory regulation processes and cognitive functions (Barch et al., 2013). The imaging dimension is  $61 \times 73 \times 61$ . The  $J = 4$  covariates include the general cognitive ability component score (Sripada et al., 2019), the psychiatric diagnostic score, age, and sex. The number of subjects is  $N = 1991$ .

Figure 3: Voxels by various methods in the brain fMRI studies. Red voxels are those selected in the all-site analysis that are reproducible in the single-site analyses, while blue voxels are those selected in the all-site analysis that are not reproducible in the single-site analyses.



Similar to the analysis of the ABIDE data, we apply IRRNN and compare it with MUA, SPM, and SVCM. We evaluate the estimation accuracy, by reporting the cross-validation of the mean squared error of the recovered response image. As shown in Table 2, our method is the most accurate in almost all the experiments. In the most extreme case, our method reduces the MSE of the alternative methods by more than 16-fold. Even in the cases where IRRNN is not the best performer, we still produces estimates with comparable accuracy. Moreover, we evaluate the selection accuracy by reporting the proportion of the reproducible voxel, as listed in Table 3 and visualized in Figure 3b. Our method again achieves the highest proportion of reproducible voxels. Table 4 reports the selected top regions and functional networks. In particular, we select a high proportion of voxels in the regions known to be associated with CA, including the parietal lobe (Haier et al., 2005; Woolgar et al., 2010; Jung and Haier, 2007), the frontal lobe (Duncan et al., 1996; Roca et al., 2010), and the precuneus (Basten et al., 2015; Jauk et al., 2015). Moreover, the memory retrieval functional network has the highest selection proportion, which is consistent with the fact that the ABCD response images used in our analysis are task-based contrast maps for activities designed to engage working memory. The selection proportion for the dorsal attention functional network is also high, which has been found in the literature to be associated with both general CA (Hilger et al., 2020) and working memory capacity (Majerus et al., 2018; Broadway and Engle, 2010; Gray et al., 2017). Other top functional networks include frontal-parietal task control (Uddin et al., 2019; Zanto and Gazzaley, 2013) and salience (Hilger et al., 2017; Liang et al., 2016), which is also consistent with the findings in existing works regarding their associations with CA and working memory. Finally, the reproducibility rate of IRRNN is much higher than that of the other methods in most of the AAL regions and networks, making IRRNN the most stable and consistent method for selection within biologically defined brain regions.

## 6 Discussion

In this work, we have presented a novel image-on-scalar regression model based on deep neural networks. From the perspective of functional data analysis, our model uses multi-layer feed-forward neural networks to approximate the spatially varying coefficient functions of the main effects, individual deviations, and noise variance. Although conceptually straightforward, our model is capable of adapting to a wide variety of spatial correlation patterns, including not only smooth transitions but also jump discontinuities across the spatial volume. We have provided an algorithm for model fitting and selection that takes advantage

Table 4: Voxel selection and reproducibility within AAL regions and functional networks in the brain fMRI data. Inside each row for each method, the first column is the name of the region/network, the second column shows the proportion of voxels inside the region/network that are selected in the all-site analysis, and the third column (in parentheses) reports the proportion of the voxels in the all-site analysis that are reproducible in the single-site analyses.

MUA		SPM		SVCM		IRRNN	
AAL regions in ABIDE							
Occ.Mid.R	11 (10)	Occ.Mid.L	13 (00)	Rec.R	13 (00)	Cal.R	17 (40)
Cal.R	10 (00)	Cal.R	12 (00)	Rec.L	12 (25)	Cal.L	15 (67)
Rec.L	09 (00)	Occ.Sup.L	10 (00)	Occ.Mid.R	10 (23)	Cun.R	12 (27)
Occ.Mid.L	07 (00)	Occ.Mid.R	10 (00)	Occ.Mid.L	09 (00)	Occ.Mid.R	12 (46)
Occ.Sup.L	06 (04)	Cun.R	08 (00)	Occ.Sup.L	08 (04)	Occ.Mid.L	07 (14)
Sup.Mot.Are.R	06 (00)	Cal.L	05 (00)	Cal.R	06 (03)	Occ.Sup.L	06 (39)
Cal.L	05 (00)	Sup.Mot.Are.R	05 (00)	Fro.Med.Orb.L	05 (38)	Cun.L	05 (35)
Rec.R	04 (00)	Cun.L	04 (00)	Fro.Sup.Orb.R	05 (83)	Fus.L	03 (06)
Cun.L	04 (00)	Rec.L	03 (00)	Tem.Pol.Mid.L	04 (00)	Lin.L	03 (21)
Occ.Inf.R	04 (00)	Rec.R	02 (00)	Sup.Mot.Are.R	04 (00)	Sup.Mot.Are.R	02 (22)
Functional networks in ABIDE							
Vis	04 (03)	Vis	06 (00)	Vis	04 (07)	Vis	07 (38)
Ven.Att	01 (00)	Ven.Att	01 (00)	Sen.Som.Han	01 (24)	Def.Mod	01 (46)
Tas.Con	01 (00)	Cin.Ope.Tas.Con	01 (00)	Cin.Ope.Tas.Con	01 (04)	Ven.Att	00 (22)
Som.Han	01 (02)	Def.Mod	00 (00)	Ven.Att	01 (00)	Cin.Ope.Tas.Con	00 (20)
Def.Mod	01 (07)	Sen.Som.Han	00 (00)	Def.Mod	01 (21)	Sen.Som.Han	00 (22)
AAL regions in ABCD							
Par.Inf.L	49 (42)	Par.Inf.L	55 (40)	Par.Inf.L	51 (42)	Par.Inf.L	51 (74)
Par.Sup.L	40 (23)	Par.Sup.L	50 (30)	Par.Sup.R	47 (46)	Fro.Mid.Orb.L	44 (00)
Pre.L	35 (59)	Par.Sup.R	47 (35)	Par.Sup.L	46 (33)	Par.Sup.L	42 (70)
Par.Inf.R	34 (56)	Pre.L	40 (61)	Par.Inf.R	39 (56)	Fro.Mid.L	36 (79)
Inf.Ope.L	33 (40)	Par.Inf.R	38 (54)	Pre.L	35 (63)	Par.Sup.R	36 (25)
Par.Sup.R	32 (13)	Fro.Inf.Ope.L	33 (37)	Pre.R	32 (71)	Fro.Inf.Ope.L	33 (73)
Pre.R	31 (65)	Pre.R	33 (68)	Fro.Inf.Ope.L	31 (31)	Fro.Sup.Orb.L	32 (97)
Pre.L	29 (59)	Fro.Mid.L	28 (49)	Fro.Mid.L	29 (53)	Pre.L	31 (83)
Lin.L	25 (12)	Pre.L	27 (53)	Pre.L	28 (57)	Fro.Mid.Orb.R	31 (96)
Fro.Mid.L	24 (42)	Sup.Mot.Are.L	24 (82)	Lin.L	23 (03)	Fro.Mid.R	29 (75)
Functional networks in ABCD							
Mem.Ret	35 (59)	Mem.Ret	40 (61)	Mem.Ret	35 (63)	Mem.Ret	31 (83)
Dor.Att	22 (43)	Dor.Att	25 (49)	Dor.Att	23 (49)	Fro.Par.Tas.Con	24 (75)
Fro.Par.Tas.Con	19 (43)	Fro.Par.Tas.Con	19 (47)	Fro.Par.Tas.Con	20 (48)	Sal	23 (75)
Sal	18 (42)	Sal	17 (47)	Sal	19 (49)	Dor.Att	21 (77)
Cin.Ope.Tas.Con	17 (53)	Cin.Ope.Tas.Con	16 (62)	Cin.Ope.Tas.Con	16 (53)	Def.Mod	14 (72)

of the high-dimensionality of the imaging data. This estimation procedure has been proved to possess theoretically guaranteed convergence properties.

In our theoretical analysis, we have derived  $L_2$  estimation error bounds for the main effects, individual deviations, and noise variance. Based on existing works on nonparametric regression with deep neural networks, our theoretical results extend them from globally smooth functions to piecewise smooth functions. Moreover, for our model selection procedure, we have demonstrated their selection consistency and proved  $L_0$  sign error bounds. In addition, we have shown the best neural network complexity, as a function of the number of images and voxels, that gives the fastest convergence rate.

In our extensive simulation studies, we have designed complex spatial images to test IRRNN against multiple existing image response regression methods. IRRNN has successfully eliminated a great proportion of the noise and learned most of the underlying heterogeneous patterns in the main effects. Moreover, IRRNN has been shown to be effective in exploiting the increasing imaging dimensions, compared to existing methods, both in terms of estimation accuracy and selection accuracy. For the analysis of brain fMRI data, IRRNN has produced more accurate estimates in the cross-validations across experimental sites. The advantage of IRRNN over the baseline methods is more prominent when the estimation task is more difficult. In addition, our model has achieved the highest selection reproducibility, as measured by the proportion of voxels that are consistently selected in the single-site analyses. Finally, as we break down the results into AAL regions and functional networks, the top regions and networks selected by IRRNN are supported by findings in existing works. The reproducibility rate in each region or network is also much higher for IRRNN than the alternative methods.

The method proposed in this article serves as an example on the integration of modern deep learning tools with classical statistical frameworks, such that data-driven, highly flexible modeling characteristics can

be enjoyed along with theoretical guarantees. We believe this strategy represents an important direction for the analysis of next-generation high-dimensional complex data. For future works, we envision multiple extensions of our proposed approach. For example, in our current setting, although the imaging resolution is high, the number of covariates is fixed at a constant value. We could extend the current theoretical results and modify the algorithm to accommodate an increasing number of covariates, which is common in applications such as imaging genetics. In addition, the images are currently assumed to be single-channel. This condition can be potentially generalized to multi-channel images, such as those in spatial transcriptomic data.

## References

- Barch, D. M., Burgess, G. C., Harms, M. P., Petersen, S. E., Schlaggar, B. L., Corbetta, M., Glasser, M. F., Curtiss, S., Dixit, S., Feldt, C., et al. (2013). Function in the human connectome: task-fMRI and individual differences in behavior. *Neuroimage*, 80:169–189.
- Barron, A. R. (1994). Approximation and estimation bounds for artificial neural networks. *Machine Learning*, 14(1):115–133.
- Basten, U., Hilger, K., and Fiebach, C. J. (2015). Where smart brains are different: A quantitative meta-analysis of functional and structural brain imaging studies on intelligence. *Intelligence*, 51:10–27.
- Bauer, B., Kohler, M., et al. (2019). On deep learning as a remedy for the curse of dimensionality in nonparametric regression. *Annals of Statistics*, 47(4):2261–2285.
- Bottou, L. (2010). Large-scale machine learning with stochastic gradient descent. In *Proceedings of COMPSTAT'2010*, pages 177–186. Springer.
- Broadway, J. M. and Engle, R. W. (2010). Validating running memory span: Measurement of working memory capacity and links with fluid intelligence. *Behavior Research Methods*, 42(2):563–570.
- Bussas, M., Sawade, C., Kühn, N., Scheffer, T., and Landwehr, N. (2017). Varying-coefficient models for geospatial transfer learning. *Machine Learning*, 106(9-10):1419–1440.
- Casey, B., Cannonier, T., Conley, M. I., Cohen, A. O., Barch, D. M., Heitzeg, M. M., Soules, M. E., Teslovich, T., Dellarco, D. V., Garavan, H., et al. (2018). The adolescent brain cognitive development (abcd) study: imaging acquisition across 21 sites. *Developmental Cognitive Neuroscience*, 32:43–54.
- Chen, H., Raskutti, G., and Yuan, M. (2019). Non-convex projected gradient descent for generalized low-rank tensor regression. *The Journal of Machine Learning Research*, 20(1):172–208.
- Chen, Y., Gao, Q., Liang, F., and Wang, X. (2020). Nonlinear variable selection via deep neural networks. *Journal of Computational and Graphical Statistics*, pages 1–9.
- Chen, Y., Wang, X., Kong, L., and Zhu, H. (2016). Local region sparse learning for image-on-scalar regression. *arXiv preprint arXiv:1605.08501*.
- Chumbley, J. R. and Friston, K. J. (2009). False discovery rate revisited: Fdr and topological inference using gaussian random fields. *Neuroimage*, 44(1):62–70.
- Craddock, C., Sikka, S., Cheung, B., Khanuja, R., Ghosh, S. S., Yan, C., Li, Q., Lurie, D., Vogelstein, J., Burns, R., Colcombe, S., Mennes, M., Kelly, C., Di Martino, A., Castellanos, F. X., and Milham, M. (2013). Towards automated analysis of connectomes: The configurable pipeline for the analysis of connectomes (c-pac). *Frontiers in Neuroinformatics*, (42).
- Di Martino, A., Yan, C.-G., Li, Q., Denio, E., Castellanos, F. X., Alaerts, K., Anderson, J. S., Assaf, M., Bookheimer, S. Y., Dapretto, M., et al. (2014). The autism brain imaging data exchange: towards a large-scale evaluation of the intrinsic brain architecture in autism. *Molecular Psychiatry*, 19(6):659–667.
- Dubois, J., Galdi, P., Paul, L. K., and Adolphs, R. (2018). A distributed brain network predicts general intelligence from resting-state human neuroimaging data. *Philosophical Transactions of the Royal Society B: Biological Sciences*, 373(1756):20170284.
- Duncan, J., Emslie, H., Williams, P., Johnson, R., and Freer, C. (1996). Intelligence and the frontal lobe: The organization of goal-directed behavior. *Cognitive psychology*, 30(3):257–303.
- Eldan, R. and Shamir, O. (2016). The power of depth for feedforward neural networks. In *Conference on learning theory*, pages 907–940. PMLR.
- Fan, J., Ma, C., and Zhong, Y. (2019). A selective overview of deep learning. *arXiv preprint arXiv:1904.05526*.
- Feng, J. and Simon, N. (2017). Sparse-input neural networks for high-dimensional nonparametric regression and classification. *arXiv preprint arXiv:1711.07592*.

- Friston, K. J. (2003). Statistical parametric mapping. In *Neuroscience databases*, pages 237–250. Springer.
- Goodfellow, I., Bengio, Y., Courville, A., and Bengio, Y. (2016). *Deep learning*. MIT press Cambridge.
- Goriounova, N. A. and Mansvelder, H. D. (2019). Genes, cells and brain areas of intelligence. *Frontiers in human neuroscience*, 13:44.
- Gray, S., Green, S., Alt, M., Hogan, T., Kuo, T., Brinkley, S., and Cowan, N. (2017). The structure of working memory in young children and its relation to intelligence. *Journal of Memory and Language*, 92:183–201.
- Hagler Jr, D. J., Hatton, S., Cornejo, M. D., Makowski, C., Fair, D. A., Dick, A. S., Sutherland, M. T., Casey, B., Barch, D. M., Harms, M. P., et al. (2019). Image processing and analysis methods for the adolescent brain cognitive development study. *NeuroImage*, 202:116091.
- Haier, R. J., Jung, R. E., Yeo, R. A., Head, K., and Alkire, M. T. (2004). Structural brain variation and general intelligence. *Neuroimage*, 23(1):425–433.
- Haier, R. J., Jung, R. E., Yeo, R. A., Head, K., and Alkire, M. T. (2005). The neuroanatomy of general intelligence: sex matters. *NeuroImage*, 25(1):320–327.
- He, K., Xu, H., and Kang, J. (2019). A selective overview of feature screening methods with applications to neuroimaging data. *Wiley Interdisciplinary Reviews: Computational Statistics*, 11(2):e1454.
- Hearne, L. J., Mattingley, J. B., and Cocchi, L. (2016). Functional brain networks related to individual differences in human intelligence at rest. *Scientific reports*, 6(1):1–8.
- Hilger, K., Ekman, M., Fiebach, C. J., and Basten, U. (2017). Efficient hubs in the intelligent brain: Nodal efficiency of hub regions in the salience network is associated with general intelligence. *Intelligence*, 60:10–25.
- Hilger, K., Fukushima, M., Sporns, O., and Fiebach, C. J. (2020). Temporal stability of functional brain modules associated with human intelligence. *Human brain mapping*, 41(2):362–372.
- Jauk, E., Neubauer, A. C., Dunst, B., Fink, A., and Benedek, M. (2015). Gray matter correlates of creative potential: A latent variable voxel-based morphometry study. *NeuroImage*, 111:312–320.
- Jung, R. E. and Haier, R. J. (2007). The parieto-frontal integration theory (p-fit) of intelligence: converging neuroimaging evidence. *Behavioral and Brain Sciences*, 30(2):135.
- Kohler, M. and Krzyżak, A. (2017). Nonparametric regression based on hierarchical interaction models. *IEEE Transactions on Information Theory*, 63(3):1620–1630.
- LeCun, Y., Bengio, Y., and Hinton, G. (2015). Deep learning. *nature*, 521(7553):436–444.
- Li, J., Huang, C., Hongtu, Z., and for the Alzheimer’s Disease Neuroimaging Initiative (2017). A functional varying-coefficient single-index model for functional response data. *Journal of the American Statistical Association*, 112(519):1169–1181.
- Li, L. and Zhang, X. (2017). Parsimonious tensor response regression. *Journal of the American Statistical Association*, 112(519):1131–1146.
- Li, X., Wang, L., Wang, H. J., and Initiative, A. D. N. (2020). Sparse learning and structure identification for ultrahigh-dimensional image-on-scalar regression. *Journal of the American Statistical Association*, pages 1–15.
- Liang, X., Zou, Q., He, Y., and Yang, Y. (2016). Topologically reorganized connectivity architecture of default-mode, executive-control, and salience networks across working memory task loads. *Cerebral cortex*, 26(4):1501–1511.
- Majerus, S., Péters, F., Bouffier, M., Cowan, N., and Phillips, C. (2018). The dorsal attention network reflects both encoding load and top-down control during working memory. *Journal of Cognitive Neuroscience*, 30(2):144–159.
- McCaffrey, D. F. and Gallant, A. R. (1994). Convergence rates for single hidden layer feedforward networks. *Neural Networks*, 7(1):147–158.

- Menary, K., Collins, P. F., Porter, J. N., Muetzel, R., Olson, E. A., Kumar, V., Steinbach, M., Lim, K. O., and Luciana, M. (2013). Associations between cortical thickness and general intelligence in children, adolescents and young adults. *Intelligence*, 41(5):597–606.
- Power, J. D., Cohen, A. L., Nelson, S. M., Wig, G. S., Barnes, K. A., Church, J. A., Vogel, A. C., Laumann, T. O., Miezin, F. M., Schlaggar, B. L., et al. (2011). Functional network organization of the human brain. *Neuron*, 72(4):665–678.
- Qiu, P. (2007). Jump surface estimation, edge detection, and image restoration. *Journal of the American Statistical Association*, 102(478):745–756.
- Rabusseau, G. and Kadri, H. (2016). Low-rank regression with tensor responses. In *Advances in Neural Information Processing Systems*.
- Raskutti, G., Yuan, M., Chen, H., et al. (2019). Convex regularization for high-dimensional multiresponse tensor regression. *The Annals of Statistics*, 47(3):1554–1584.
- Roca, M., Parr, A., Thompson, R., Woolgar, A., Torralva, T., Antoun, N., Manes, F., and Duncan, J. (2010). Executive function and fluid intelligence after frontal lobe lesions. *Brain*, 133(1):234–247.
- Schmidt-Hieber, J. et al. (2020). Nonparametric regression using deep neural networks with relu activation function. *Annals of Statistics*, 48(4):1875–1897.
- Schnack, H. G., Van Haren, N. E., Brouwer, R. M., Evans, A., Durston, S., Boomsma, D. I., Kahn, R. S., and Hulshoff Pol, H. E. (2015). Changes in thickness and surface area of the human cortex and their relationship with intelligence. *Cerebral cortex*, 25(6):1608–1617.
- Shi, R. and Kang, J. (2015). Thresholded multiscale gaussian processes with application to bayesian feature selection for massive neuroimaging data. *arXiv preprint arXiv:1504.06074*.
- Simard, I., Luck, D., Mottron, L., Zeffiro, T. A., and Soulières, I. (2015). Autistic fluid intelligence: Increased reliance on visual functional connectivity with diminished modulation of coupling by task difficulty. *NeuroImage: Clinical*, 9:467–478.
- Song, M., Zhou, Y., Li, J., Liu, Y., Tian, L., Yu, C., and Jiang, T. (2008). Brain spontaneous functional connectivity and intelligence. *Neuroimage*, 41(3):1168–1176.
- Sripada, C., Rutherford, S., Angstadt, M., Thompson, W. K., Luciana, M., Weigard, A., Hyde, L. H., and Heitzeg, M. (2019). Prediction of neurocognition in youth from resting state fmri. *Molecular Psychiatry*, pages 1–9.
- Stone, C. J. (1982). Optimal global rates of convergence for nonparametric regression. *The annals of statistics*, pages 1040–1053.
- Sun, W. W. and Li, L. (2017). Store: sparse tensor response regression and neuroimaging analysis. *The Journal of Machine Learning Research*, 18(1):4908–4944.
- Telgarsky, M. (2016). Benefits of depth in neural networks. In *Conference on learning theory*, pages 1517–1539. PMLR.
- Tzourio-Mazoyer, N., Landeau, B., Papathanassiou, D., Crivello, F., Etard, O., Delcroix, N., Mazoyer, B., and Joliot, M. (2002). Automated anatomical labeling of activations in spm using a macroscopic anatomical parcellation of the mni mri single-subject brain. *Neuroimage*, 15(1):273–289.
- Uddin, L. Q., Yeo, B. T., and Spreng, R. N. (2019). Towards a universal taxonomy of macro-scale functional human brain networks. *Brain topography*, 32(6):926–942.
- Woolgar, A., Parr, A., Cusack, R., Thompson, R., Nimmo-Smith, I., Torralva, T., Roca, M., Antoun, N., Manes, F., and Duncan, J. (2010). Fluid intelligence loss linked to restricted regions of damage within frontal and parietal cortex. *Proceedings of the National Academy of Sciences*, 107(33):14899–14902.
- Yoon, Y. B., Shin, W.-G., Lee, T. Y., Hur, J.-W., Cho, K. I. K., Sohn, W. S., Kim, S.-G., Lee, K.-H., and Kwon, J. S. (2017). Brain structural networks associated with intelligence and visuomotor ability. *Scientific reports*, 7(1):1–9.
- Yu, C., Li, J., Liu, Y., Qin, W., Li, Y., Shu, N., Jiang, T., and Li, K. (2008). White matter tract integrity and intelligence in patients with mental retardation and healthy adults. *Neuroimage*, 40(4):1533–1541.

- Yu, S., Wang, G., Wang, L., and Yang, L. (2020). Multivariate spline estimation and inference for image-on-scalar regression. *Statistica Sinica*.
- Yue, Y., Loh, J. M., and Lindquist, M. A. (2010). Adaptive spatial smoothing of fmri images. *Statistics and its Interface*, 3:3–13.
- Zanto, T. P. and Gazzaley, A. (2013). Fronto-parietal network: flexible hub of cognitive control. *Trends in cognitive sciences*, 17(12):602–603.
- Zhao, P. and Yu, B. (2006). On model selection consistency of lasso. *The Journal of Machine Learning Research*, 7:2541–2563.
- Zhou, S. (2010). Thresholded lasso for high dimensional variable selection and statistical estimation. *arXiv preprint arXiv:1002.1583*.
- Zhu, H., Fan, J., and Kong, L. (2014). Spatially varying coefficient model for neuroimaging data with jump discontinuities. *Journal of the American Statistical Association*, 109(507):1084–1098.